PROPERTIES OF INDIUM-ARSENIDE MEASURED BY LOW TEMPERATURE PHOTOLUMINESCENCE

by

YVES LACROIX
B.Sc.(Honours) S.Sp. Physics, Queen's University, 1991

THESIS SUBMITTED IN PARTIAL FULFILMENT OF
THE REQUIREMENTS FOR THE DEGREE OF
DOCTOR OF PHILOSOPHY
in the Department
of
PHYSICS

SIMON FRASER UNIVERSITY
April, 1996

Approval Page

NAME: Yves Lacroix
DEGREE: Doctor of Philosophy (Physics)
TITLE OF THESIS: Properties of Indium-Arsenide Measured by Low Temperature Photoluminescence

EXAMINING COMMITTEE:

CHAIR: Jeff Dahn

Mike Thewalt
Senior Supervisor
Professor of Physics

George Kirczenow
Professor of Physics

Simon Watkins
Assistant Professor of Physics

John Bechhoefer
Internal External Examiner
Professor of Physics

Alain Roth
External Examiner
Senior research officer, C.N.R.C.

DATE APPROVED: 26 April 1996

PARTIAL COPYRIGHT LICENSE

I hereby grant to Simon Fraser University the right to lend my thesis, project or extended essay (the title of which is shown below) to users of the Simon Fraser University Library, and to make partial or single copies only for such users or in response to a request from the library of any other university, or other educational institution, on its own behalf or for one of its users. I further agree that permission for multiple copying of this work for scholarly purposes may be granted by me or the Dean of Graduate Studies. It is understood that copying or publication of this work for financial gain shall not be allowed without my written permission.

Title of Thesis/Project/Extended Essay

Properties of Indium Arsenide Measured by Low Temperature Photoluminescence.

Author: _____
(signature)

_____
(name)

6 May 1996
(date)

Abstract

Low temperature (1.4K) photoluminescence studies as well as reflectance and transmittance measurements were performed on high purity epitaxial InAs grown by MOCVD. The identification of photoluminescence spectral features never before observed, with line widths roughly a thousand times narrower than previously published results by other groups, was the main focus of this work.. Among the identifications are the exciton-polariton at 415.65±0.01 meV, a donor-bound exciton transition with a binding energy of 0.42 meV, and three different acceptor impurities observed from donor-acceptor-pair band transitions as well as from the acceptor-bound exciton recombination. Other physical properties measured from the spectrum of InAs are the conduction band effective mass and g-factor, (from the magnetic field dependence), and the longitudinal optic phonon energy.

This work also involved the design and development of a cryogenic Fourier transform interferometer for emission measurements in the mid-infrared. It was used to study a deep (~375 meV) luminescence band of unknown origin, related to drastic temporal changes in the band-edge photoluminescence intensity of InAs.

Acknowledgements

This work would not have been possible without the input of several other researchers at Simon Fraser University. Dr. Chuong Tran and Dr. Simon Watkins were responsible for producing the material which is the focus of this study. Professor Mike Thewalt's invaluable knowledge and experimental insight were just a fraction of his contribution. I am grateful for his support as well as for the trust he invested in me.

A great big thanks to everyone who helped through technical work, discussions, proof-reading and moral support: Sakura, Richard, Dale, Jennifer, Serguei, James, and many others. The figures in this thesis were all produced using Splot, an OS/2 software developed by Dr. Thomas Steiner.

À ma famille, dont j'ai dû demeurer séparé, votre amour et votre confiance restent la fondation de tout ce que j'ai entrepris jusqu'à présent. Je vous remercie infiniment. Oui, toi aussi Nicholas.

Table of Contents

Approval Page ii
Abstract iii
Acknowledgements iv
List of Tables vii
List of Figures viii
List of Abbreviations ix

CHAPTER 1 - INTRODUCTION 1

WHAT IS INDIUM-ARSENIDE? 1
WHAT IS THIS ABOUT? 2
THE THESIS 3

CHAPTER 2 - FROM ELECTRONS TO EXCITONS 4

ELECTRONS 5
Electronic States in a Semiconductor *5*
Electron in Vacuum 5
Electrons in a crystal 6
Effective mass, holes and the dielectric constant 10
Real Band Structures *11*
Zincblende structure 12
EXCITONS AND IMPURITIES 14
The Life of an Exciton *15*
Impurities *18*
Shallow donors 18
Shallow acceptors 20
Donor-acceptor-pairs 21
Excitons Bound to Neutral Donors and Acceptors *23*
Identification of Impurity Species *24*
THE TOTAL ENERGY PICTURE 25
THE EFFECT OF AN EXTERNAL MAGNETIC FIELD 27
CARRIER MOBILITY 27

CHAPTER 3 - EXPERIMENTAL TECHNIQUES 29

GROWTH TECHNIQUE - MOCVD 29
GROWTH OF INAS FOR PHOTOLUMINESCENCE STUDIES 32
LOW TEMPERATURE PHOTOLUMINESCENCE SETUP 33
FOURIER TRANSFORM SPECTROSCOPY 36
MID-INFRARED TECHNIQUES 38
Cold Filter Method *40*
Cryogenic Fourier Transform Interferometer *41*

CHAPTER 4 - THE SPECTRUM OF INAS 48

DONOR-ACCEPTOR PAIR BANDS 49
ACCEPTOR-BOUND EXCITONS 52

Acceptors A_1 and A_2 52
Acceptor A_3 55
FREE EXCITON (POLARITON) 57
DONOR-BOUND EXCITONS 61
MAGNETIC FIELD DEPENDENCE 63
BROAD BANDS 67
Samples grown on GaAs substrates 69
Deep Time-Dependent Band 70
RESULTS SUMMARY 73

CHAPTER 5 - CONCLUSIONS **74**

INAS HIGH MOBILITY APPLICATIONS 74
INAS IN INFRARED, OPTO-ELECTRONIC APPLICATIONS 75
WHERE TO GO FROM HERE 76
Exciton Physics 76
Impurity Identification 76
InGaAsSb and Related Compounds 77

APPENDIX A **78**

APPENDIX B **79**

REFERENCES **81**

List of Tables

TABLE I. THE CHARACTER TABLE FOR ZINCBLENDE STRUCTURE 13
TABLE II. THEORETICAL ENERGY SPECTRUM OF ACCEPTOR IMPURITIES IN INAS 20
TABLE III. PHYSICAL QUANTITIES OBTAINED FROM THE INAS SPECTRA PRESENTED IN THIS THESIS 57
TABLE IV. PHOTOLUMINESCENCE PEAK POSITIONS AT 1.4K AND 0 TESLA 64
TABLE V. LIST OF SAMPLES USED FOR THE THESIS FIGURES. 78

List of Figures

FIGURE 1. THE DISPERSION RELATION OF A FREE ELECTRON IN VACUUM. 6

FIGURE 2. THE KRONIG-PENNEY MODEL ENERGY DISPERSION 8

FIGURE 3. PSEUDO-POTENTIAL CALCULATION OF THE BAND STRUCTURE OF INAS [13]. 11

FIGURE 4. BAND-GAP REGION OF THE INAS BAND STRUCTURE 14

FIGURE 5. INITIAL STATE OF (A) BAND-TO-BAND RECOMBINATION AND (B) EXCITON RECOMBINATION 16

FIGURE 6. QUASI-HYDROGENIC LEVELS OF THE NEUTRAL DONOR 18

FIGURE 7. NEUTRAL ACCEPTOR STATES 20

FIGURE 8. DONOR-ACCEPTOR PAIR STATES. (A) NEUTRALISED (B) IONISED GROUND STATE 21

FIGURE 9. AN EXCITON BOUND TO A NEUTRAL DONOR (D^0,X) 23

FIGURE 10. AN EXCITON BOUND TO A NEUTRAL ACCEPTOR (A^0,X) 24

FIGURE 11. THE TOTAL ENERGY PICTURE. 26

FIGURE 12. MOCVD: SCHEMATIC OF THE HYDROGEN "BUBBLERS" 30

FIGURE 13. MOCVD: SCHEMATIC OF THE REACTOR CHAMBER 31

FIGURE 14. MOCVD: RELAXED BUFFER LAYER GROWTH PROFILE 33

FIGURE 15. PHOTOLUMINESCENCE: TOP VIEW OF THE SAMPLE CHAMBER IN THE LIQUID HELIUM CRYOSTAT 34

FIGURE 16. PHOTOLUMINESCENCE: COMPONENTS OF A FOURIER TRANSFORM SPECTROMETER 36

FIGURE 17. COLD FILTER METHOD 40

FIGURE 18. CRYOGENIC INTERFEROMETER: THE OPTICAL PATH WITH COLD COMPONENTS 42

FIGURE 19. CRYOGENIC INTERFEROMETER: THE LIQUID NITROGEN COOLING SYSTEM 44

FIGURE 20. CRYOGENIC INTERFEROMETER: PERSPECTIVE DIAGRAMMATIC VIEW 46

FIGURE 21. CRYOGENIC INTERFEROMETER: PICTURE 47

FIGURE 22. SPECTRUM OF INAS AT 1.4 K. (A) SAMPLE CONTAINING ONE ACCEPTOR, A_2. (B) SAMPLE CONTAINING TWO ACCEPTORS, A_1 AND A_3 50

FIGURE 23. THE EXCITATION POWER DEPENDENCE OF THE TRANSITIONS SHOWN IN FIGURE 22(B) 51

FIGURE 24. HIGH RESOLUTION SPECTRUM OF THE NEUTRAL-ACCEPTOR-BOUND EXCITON 53

FIGURE 25. AN EXPANDED VIEW OF THE EXCITONIC ENERGY REGION 59

FIGURE 26. EXCITONIC PHOTOLUMINESCENCE AT A) 4.2 K AND B) 1.4 K 60

FIGURE 27. SUBSTRUCTURE OF THE NEUTRAL-DONOR-BOUND EXCITON 62

FIGURE 28. THE EXCITONIC REGION AT 1.4K UNDER A MAGNETIC FIELD OF 1 TESLA 66

FIGURE 29. PHOTOLUMINESCENCE OF THE VARIOUS BROAD BANDS 68

FIGURE 30. EXCITATION DENSITY DEPENDENCE OF THE DEEP 374 MEV BAND 72

FIGURE 31. THE MID-INFRARED SPECTRUM OF WATER 79

FIGURE 32. BLOW-UP OF FIGURE 31 ON A FEW LINES TO DEMONSTRATE THE INSTRUMENTAL RESOLUTION. . 80

List of Abbreviations

A ---------- Acceptor
A^- ---------- Ionised acceptor
A^0 ---------- Neutral acceptor
(A^0,X) ---------- Neutral-acceptor-bound exciton (principal)
$(A^0,X\ 2h)$ ---------- Neutral-acceptor-bound exciton (2 hole)
D ---------- Donor
D^+ ---------- Ionised donor
D^0 ---------- Neutral donor
(D^0,X) ---------- Neutral-donor-bound exciton
DAP ---------- Donor-acceptor pair
DS ---------- Dispersion spectroscopy
(e,A^0) ---------- Free electron to neutral acceptor
(e,h) ---------- Electron-hole pair, or band-to-band
E_B ---------- Binding energy
E_{BA} ---------- Acceptor binding energy
E^{exc}_{BA} ---------- Neutral-acceptor-bound exciton binding energy
E_{BD} ---------- Donor binding energy
E^{exc}_{BD} ---------- Neutral-donor-bound exciton binding energy
E_{Bex} ---------- Exciton binding energy
E_{DAP} ---------- Donor-acceptor pair recombination energy
E_G ---------- Band gap energy
E_{Gex} ---------- Excitonic band gap energy
ΔE_{12} ---------- Neutral acceptor $1S_{3/2}$ to $2S_{3/2}$ energy difference
FTS ---------- Fourier transform spectroscopy
MOCVD ---------- Metal organic chemical vapour deposition
TBA ---------- Tertiarybutylarsene
TMI ---------- Trimethylindium
X ---------- Exciton (polariton)

CHAPTER 1 - INTRODUCTION

It was a dark and rainy day in Vancouver. As usual. I had finally cracked the infamous indium-arsenide case. I had worked on it day in and day out for as long as I could remember. It had been messy. I felt good. But it wasn't over. I knew too much...

WHAT IS INDIUM-ARSENIDE?

Hopefully, the next eighty pages or so will answer a portion of that question. In brief, indium-arsenide is a solid semiconducting crystal. It has a grey metallic colour and is very brittle. It distinguishes itself from other common semiconductors like silicon (Si) or gallium-arsenide (GaAs), by its *narrow forbidden energy gap.* This means that optical transitions associated with this material will occur in the mid-infrared region of the light spectrum, instead of the near-infrared region like Si or GaAs. For that reason, opto-electronic applications using indium-arsenide, often alloyed with antimony and/or gallium, are typically heterostructure devices for infrared emission or detection.

Another distinctive characteristic of InAs is its intrinsically high electron mobility, making it a choice material for high-sensitivity Hall-sensors. A more contextual discussion of present and future physics and applications, is included as part of the conclusions at the very end of this thesis. By then, the terminology as well as some of the general semicon-

ductor physics background will have been introduced, and a better appreciation for the research reported here will also be possible.

WHAT IS THIS ABOUT?

Considering the importance of InAs in heterostructure technology, it is quite striking to discover how little is known of either the properties of its impurities, or of methods for their detection and characterisation. This is due in part to the lack of well-resolved photoluminescence studies that can, as in Si, GaAs or InP, determine impurity species as well as (to a lesser degree of certainty) concentration.

In the past year renewed progress has been possible in the optical characterisation of epitaxial InAs due to the recent availability of high purity material grown by metal organic chemical vapour deposition (MOCVD).

Recently published reports [1][2][3], by co-researchers and myself have shown photoluminescence spectra of residually n-type epitaxial InAs with identifiable excitonic lines roughly a thousand times narrower than previously published results by other groups [4][5][6][7][8]. This thesis summarises these results and presents new measurements, interpretations and motivations. It attempts to give an up-to-date report on the InAs photoluminescence research at the time of this writing, as well as provide guidance for those who will continue this work.

THE THESIS

This manuscript consists essentially of three chapters. For those readers that have a good background in semiconductor photoluminescence measurements, chapter four is mainly concerned with the results and interpretations of the InAs photoluminescence spectrum. The content of that chapter is also the core of a research paper [9] submitted to the Journal of Applied Physics.

Chapter three describes the experimental aspects of the research. For those interested in the techniques of growth and characterisation used, this is where they can be found. Particularly, the design of a cryogenic Fourier transform interferometer, conceived during my doctorate, is discussed there.

For most readers however, a review of the important physical concepts is required in order to appreciate the results presented in chapter four. Chapter two is a guide through relevant elements of semiconductor physics from the basic electron in free space, up to a general description of excitons in semiconductors. From there, a context appropriate to the results chapter should be achieved. The approach taken in chapter two is based, in part, on many years of trying to find the best way to explain what I do to people outside this field, and also to students who have joined our research group.

CHAPTER 2 - FROM ELECTRONS TO EXCITONS

Understanding the collective behaviour of 10^{24} interacting electrons and atoms which in turn interact with photons seems like quite an impossible task. Yet this is the problem semiconductor physicists have been tackling for the past seventy years or so. Like all the impossible problems that have been "solved" in the history of science, a certain amount of faith in the initial assumptions was necessary in order to further develop the theories. Once a 'good' model was found that reproduced nature, it could be used to progress towards the next level of understanding. Of course careful measurement and a proper interpretation of nature is necessary in order to chose a "good" model and that is the principal function of experiments in physics.

This thesis presents new measurements, as well as physical interpretations of these measurements, based on the current understanding of semiconductor physics and more specifically of "exciton" physics. In chapter four, results from the study of excitons in InAs are presented and analysed, from which physical properties of InAs are inferred. Our goal, which will be repeated throughout this work, will be to correctly identify the physical processes responsible for features of the photoluminescence spectra.

In this chapter, emphasis is given to those aspects of the physics of semiconductors relevant to this study. Rigor is not the objective here and for more detail on specific concepts, references are given.

ELECTRONS

Before I can start talking of excitons, many terms need to be defined and developed in order to set the proper context. I will first guide the reader starting from the simple single electron system, to a description of the states of electrons inside a semiconductor (for various approaches, see for example Kittel [10], Ashcroft and Mermin [11] or Harrison [12]). Then to set the stage for the topic of this thesis, I will discuss the actual band structure of InAs.

Electronic States in a Semiconductor

Electron in Vacuum

The free electron Schrödinger equation,

$$\nabla^2\psi + \frac{2m_0}{\hbar^2}E\psi = 0 \tag{2.1}$$

has solutions that can be described as *electron waves* given by

$$\psi(\mathbf{r}) = Ae^{\pm i\mathbf{k}\cdot\mathbf{r}} \tag{2.2}$$

The *wave vector* $\mathbf{k}$ is related to the electron momentum by

$$\mathbf{p} = \hbar\mathbf{k} \tag{2.3}$$

and hence the energy dispersion of the free electron can be written as

$$E = \frac{p^2}{2m_0} = \frac{\hbar^2 k^2}{2m_0}, \tag{2.4}$$

which describes a simple parabola, as shown in Figure 1.

The dispersion relation is often the focus of many discussions in semiconductor physics. When it is known, the wave vector readily gives the energy of the state, as well the mass of the particle, which from (2.4) can be related to the curvature of the dispersion by

$$m_0 = \frac{\hbar^2}{\frac{\partial^2 E}{\partial k^2}}. \tag{2.5}$$

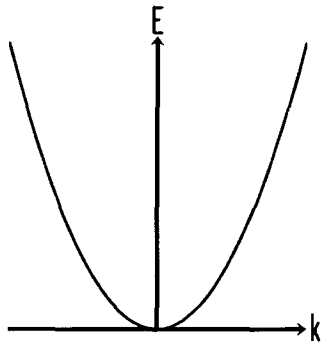

Figure 1. The dispersion relation of a free electron in vacuum.

If the dispersion is parabolic, then the defined mass is a constant, and familiar classical Newtonian theory can be used. We will return to this later in the context of effective mass theory.

Electrons in a crystal

If we now put the electron inside a crystal, the Schrödinger equation becomes

$$\nabla^2\psi + \frac{2m_0}{\hbar^2}(E(\mathbf{k}) - V(\mathbf{r}))\psi = 0, \tag{2.6}$$

where $V(\mathbf{r})$ describes the periodic potential of the crystal formed of positive atoms arranged in a lattice. The solutions to this equation are called *Bloch functions* (Bloch, 1928)

and have the form

$$\psi_n(\mathbf{k},\mathbf{r}) = u_n(\mathbf{k},\mathbf{r})e^{i\mathbf{k}\cdot\mathbf{r}}. \tag{2.7}$$

Like electrons in vacuum, *Bloch functions* are spatial plane waves, except that the *electron wave* is now modulated by a periodic function $u_n(\mathbf{k},\mathbf{r})$ which reflects the periodicity of the lattice. The subscript n is called the *band* index for reasons which will become clear in a moment.

One does not have to solve this problem for a very complex system in order to obtain the general picture from which much insight can be gained. Imagine a one-dimensional crystal of positive atoms separated by a lattice constant a. The lattice potential can be approximated by a function which is periodic in $a=a_1+a_2$, vanishing for a distance a_1 and then equal to a constant V_0 for a distance a_2 (Kronig and Penney, 1932). For the electron in the lattice the potential barrier V_0 represents the region between atoms, since the negatively charged electron reduces its energy when it sits on top of the positive atoms. The dispersion relation for this simple system with V_0=10 eV, a_1=5.5 Å and a_2=0.5 Å is shown in Figure 2. The free electron parabola is also shown (dashed curve) for comparison. Because the solution is periodic in $\mathbf{k}$, with period $2\pi/a$, the usual method of displaying the dispersion relation is to just show the *wave vector* region from zero to π/a (in three dimensions, this region is called the *Brillouin zone*). There are several solutions for the same value of k, corresponding to different values of the *band index* in the *Bloch functions*.

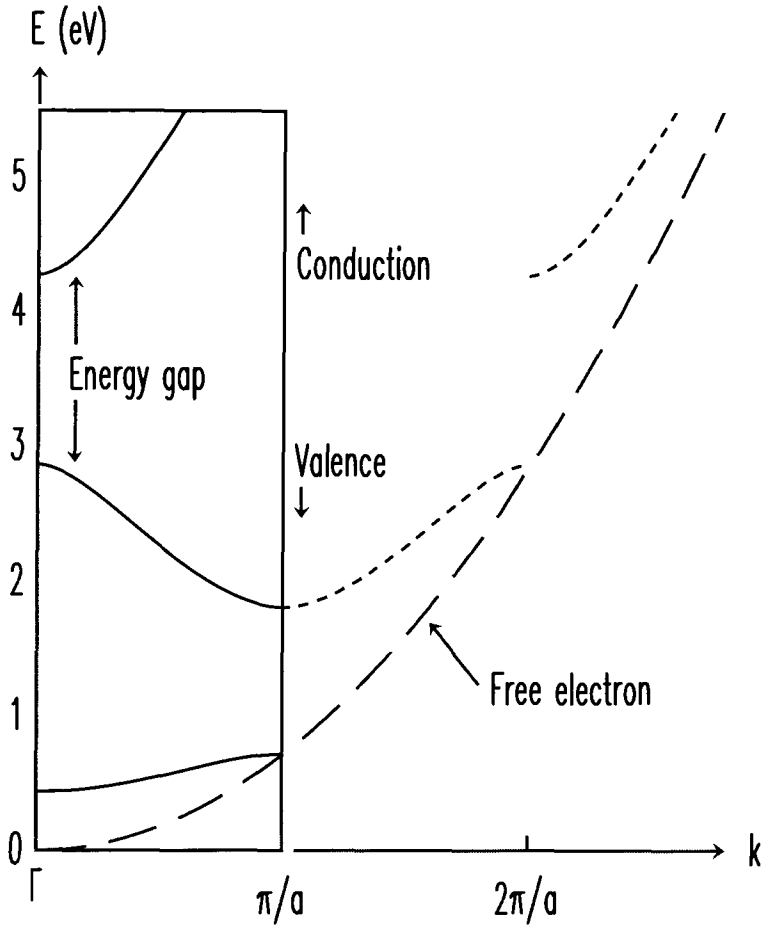

Figure 2. The Kronig-Penney model energy dispersion (V_0=10eV, a_1=5.5Å, a_2=0.5Å) plotted against the free electron dispersion. The dotted lines just show a continuation of the k-periodic solutions (solid lines). The locations of the band gap, the conduction and valence bands are shown for the case of a four electron per atom system..

It is clear from the Figure 2 that the effect of the crystal lattice on the electron has been to introduce *gaps* in the energy spectrum at values of $k=\pi/a$, $2\pi/a$ and so on. At those values of k, the periodicity of the electron wavefunctions is the same as that of the lattice.

As electrons are added to the system, they occupy the next available lowest energy state. Two electrons (of opposite spin) can occupy a state given by the band index n and wave vector k. (There are as many k states in a band as there are unit cells in the crystal.)

One can imagine that they fill the crystal as harmonics on a guitar string do: the first state, with k=0, is flat, the next state has one node, the next two, and so on. When the state with the lattice periodicity is reached, two states are available. One is *in phase* with the lattice, the other *out of phase.* In the former, each node of the electron wavefunction sits between each atom. This state is more bound to the lattice than its counterpart and its energy is reduced. The *unbound* state has a higher energy by an amount given by the energy gap, or *band gap* as we shall call it from now. We shall also us the words *conduction* and *valence* bands, to denote the ensemble of states above and below the band gap, respectively (as shown in Figure 2).

In semiconductors, the valence band is completely filled and the conduction band is empty. To add another electron, or simply to move one (change its wave vector) requires an input of energy greater than the band gap energy. If the gap is very large, then the electrons cannot move and the material is an insulator (the diamond state of carbon for example). For semiconductors, the band gap is smaller than ~2 eV but not zero. This is small enough for carriers to be thermally excited across the band gap at room temperature, giving the material (semi) conducting properties, which disappear at low temperature.

The dispersion relation (or band structure) for more complex three dimensional systems are fundamentally the same as the simple example just given. In some cases the next available state above the gap turns out to be at a different wave vector than the state below the gap. These are called *indirect band gap semiconductors*; examples include Si and Ge. InAs, like most other III/V semiconductors (compounds from valence groups III and V), are *direct semiconductors.*

Effective mass, holes and the dielectric constant

When an electron is promoted from the valence band into the conduction band, an empty state is created. This empty state is called a *hole*. Just as a drop of water is not a useful concept below the surface of the liquid, and an air bubble ceases to exist above that surface, in the valence band the concept of electrons loses its usefulness. We speak there of hole states. And like an air bubble which floats to the surface, the hole's energy minimum is toward the top of the valence band, opposite to the electron's.

In the first section, for a parabolic dispersion, we defined the mass of the electron by the curvature of the band. Notice that in Figure 2, the valence band maximum as well as the conduction band minimum are nearly parabolic. Whenever this is true, an effective mass for the electron (or the hole) can be defined analogous to equation (2.5). This is called the *effective mass approximation* and it enables electrons in a crystal to be treated as if they were simply free electrons, with different (effective) masses m^*. If we were to consider an *electron* at the top of the valence band, its mass would be negative since the curvature is negative. But a valence band hole moves opposite to a conduction electron as a reaction to an external force (since it is the absence of an electron, ex: gravity down, bubble goes up). So its "mass" is already negative. The definition of the effective mass then gives a positive mass for the hole. The electron and the hole effective masses, from the conduction band and the valence band curvatures respectively, are defined by

$$m_e^* = \frac{\hbar^2}{\left.\frac{\partial^2 E}{\partial k^2}\right|_{E_{cond}}} \qquad m_h^* = -\frac{\hbar^2}{\left.\frac{\partial^2 E}{\partial k^2}\right|_{E_{val}}}. \tag{2.8}$$

In the framework of effective mass theory, the charge interactions are also treated as if in vacuum. The differences due to the dielectric properties of the material are absorbed in the dielectric constant ε, which replaces the permittivity of free space. Using these approximations, one can then tackle more realistic systems.

Real Band Structures

The pseudo-potential calculation [13] of the band structure of InAs is shown in Figure 3. Since the wave vector can now point in all directions, principal directions are chosen along which the dispersion is calculated. For example, starting from the <000> or Γ (**k**=(0,0,0)) point, the energy dispersion is plotted along the **k**=(1,0,0) vector to the edge of the Brillouin zone, denoted X or <100>. Other directions are L <111> and K <110>.

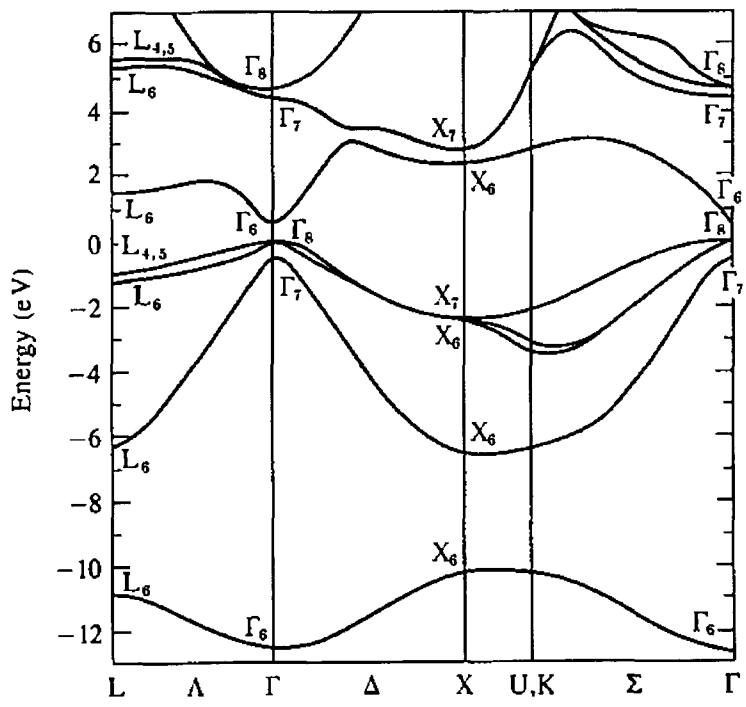

Figure 3. Pseudo-potential calculation of the band structure of InAs [13].

Because the dispersion will differ with wavevector orientation, it is usually necessary to introduce a tensor relation for the effective mass (a **k**-dependent effective mass). For simplicity, we will assume isotropic effective masses in this discussion. This approximation has been shown to be valid for conduction electrons in InAs.

Since InAs is a direct gap semiconductor and the photon energies used for the experiments in this work are of the order of the band gap, only the band structure close to the band gap, both in energy and wave vector, is important. The electronic states beyond have a negligible effect. So from here on, only the Γ point (Brillouin zone centre) of the band structure is considered.

Zincblende structure

The labels at various points in the band structure of Figure 3 (ex: L_6, Γ_8 etc...) denote the group symmetry of the electron (or hole) states. InAs crystallises in the zincblende structure which has T_d^2 point group symmetry, and the subscripts of the above labels represent specific irreducible representations of T_d^2. The character table for this group is given in Table I, but we shall only pay attention to the first column of numbers which corresponds to the degeneracy of the irreducible representation.

The "unbound electron" states of the conduction band are s-like. They are not affected by the cubic symmetry of the crystal and therefore preserve the whole symmetry of the crystal structure (Γ_1). The actual spin-degenerate states are represented by Γ_6. The valence band describing the hole states is more complicated.

Table I. The character table for T_d^2, the point group of the zincblende structure.

	E	$\underline{E}$	$8C_3$	$8\underline{C}_3$	$3C_2$ $3\underline{C}_2$	$6S_4$	$6\underline{S}_4$	$6\sigma d$ $6\underline{\sigma} d$
Γ_1	1	1	1	1	1	1	1	1
Γ_2	1	1	1	1	1	-1	-1	-1
Γ_3	2	2	-1	-1	2	0	0	0
Γ_4	3	3	-1	-1	2	0	0	0
Γ_5	3	3	0	0	-1	-1	-1	1
Γ_6	2	-2	1	-1	0	$\sqrt{2}$	$-\sqrt{2}$	0
Γ_7	2	-2	1	-1	0	$-\sqrt{2}$	$\sqrt{2}$	0
Γ_8	4	-4	-1	1	0	0	0	0

InAs is a compound of two elements with valences three and five. Each atom with its four neighbours looks like a CH_4 molecule. Of the eight electronic states forming the filled valence shell, two are tightly bound s-states states represented by Γ_6 (see bottom of Figure 3) and need not be considered in our treatment. The degeneracy of the other six p-like states is lifted by a spin-orbit interaction into two levels with representations Γ_7 and Γ_8. The Γ_8 level is four-fold degenerate with total spin 3/2, and the Γ_7 level is two-fold degenerate with spin 1/2. The latter is referred to as the *split-off* band.

A sketch of the band-gap region summarising the above is shown in Figure 4. The pseudo-potential calculation of the band structure gives values of -0.43 eV for the split-off band energy maximum and 0.37 eV for the conduction band minimum (or band gap). Since the split-off energy is so large in this material, the split-off valence band can also be neglected in the description of hole states. Also, notice that away from the Γ point, the Γ_8 band is no longer four-fold degenerate. It splits in two bands due to crystal anisotropy and these bands have different curvatures. They are known as heavy and light hole bands.

Now that the nature of electron and hole states in InAs is established, their interactions with each other and with impurities in the crystal can be considered.

EXCITONS AND IMPURITIES

Excitons are intrinsic entities formed by individually bound electrons and holes, but are not collective states of the crystal. Hence they cannot truly be described in the context of the band structure. The same is true of impurities since they are, by definition, not intrinsic manifestations of the pure ideal semiconductor crystal. However, the electrons and holes which form the excitons or interact with the impurities are well described by the band structure states developed in the previous sections. An exciton, for example, is formed of an electron in the conduction band of symmetry Γ_6 and a hole in the valence band of symmetry Γ_8, and therefore has $(\Gamma_6 \times \Gamma_8) = \Gamma_3 + \Gamma_4 + \Gamma_5$ symmetries. For that reason, we shall continue to use the band structure picture in this section.

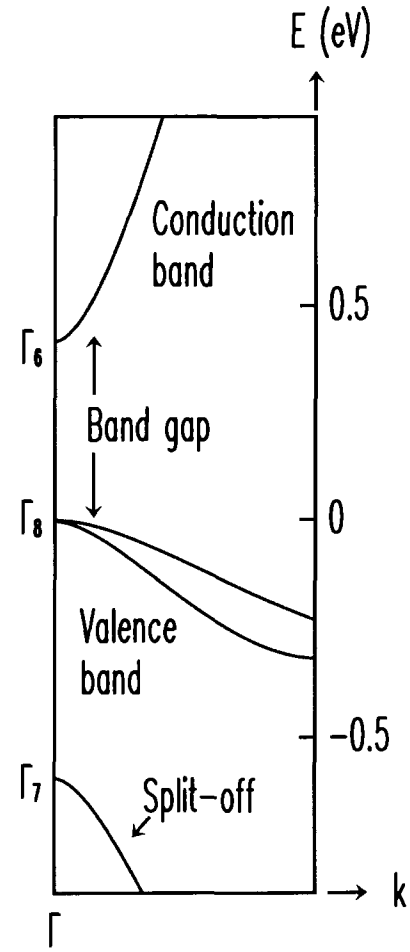

Figure 4. Band-gap region of the InAs band structure (a blow-up sketched of Figure 3, in an arbitrary wave vector direction). The zero of energy is the top of the valence band.

In order to explain the exciton phenomenon, a good approach is to understand how it is born (creation), how it lives, and how it dies (recombination).

The Life of an Exciton

One way to create an electron-hole pair in a pure semiconductor crystal is to give a valence electron enough energy to be promoted to the conduction band. In this process, both a free electron and a free hole are created. If the initial energy is larger than the band gap, the two particles quickly relax to the valence and conduction band extrema via interaction with the lattice. At high temperature, the electron then very quickly recombines with the hole, aborting the formation of excitons, and emitting a photon of energy equal to the band gap. The initial state in this process, called band-to-band recombination, is sketched in Figure 5(a). In narrow band gap semiconductors, because of the presence of thermally activated carriers, the dominant recombination process is often to transfer the energy to another electron or hole instead of a photon.

At low temperature however, with much fewer collisions, the electron and hole have the time to sense each other's Coulomb potential and bind together, similar to an electron binding to a proton to form a hydrogen atom. Thus an exciton is born. This metastable complex is free to move throughout the crystal, and its lifetime is inversely proportional to the spatial overlap of the electron and hole wavefunctions. The exciton eventually annihilates by recombination of the electron and hole. This process causes the emission of a photon, with energy given by the band gap energy minus the exciton binding energy.

It is important to realise that the exciton recombination energy is below that of the band gap of the semiconductor. This is sketched in Figure 5(b), superimposed on the valence and conduction bands, to show that an electron and hole reduce their energy when

they form an exciton. In photoluminescence measurements of high purity materials, at low temperature, the free exciton recombination is the highest energy feature in the spectrum. Hence its energy position is often labelled *the excitonic band gap* (the free carrier, or band-to-band recombination energy gives the *electronic* band gap).

Because of the complexity of the valence band, as described in the previous section, even in the context of effective mass theory the treatment of the exciton as a two-particle hydrogen system is a gross approximation. The Hamiltonian for the relative electron-hole motion is (neglecting the electron spin)

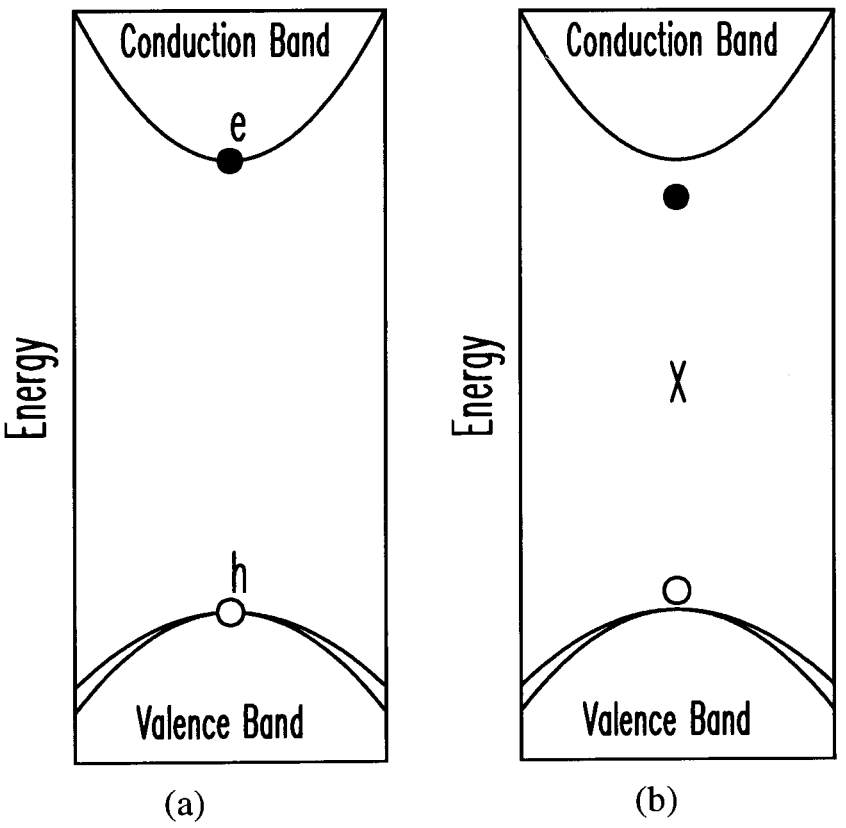

Figure 5. Schematic initial state representation of (a) band-to-band recombination and (b) exciton recombination. The labels represent a conduction band electron (e), a valence band hole (h) and an exciton (X). In these and the other diagrams, open circles are holes, and filled circles are electrons.

$$H_{ex}(\mathbf{p}) = \left(\frac{p^2}{2m_e^*} - \frac{e^2}{\varepsilon r} \right) \mathbf{I} - H_v(\mathbf{p}), \tag{2.9}$$

where **p** is the relative electron-hole momentum, m_e^* is the electron effective mass, ε is the static dielectric constant, r is the electron-hole distance, **I** is the 6×6 unit matrix, and H_v is the 6×6 matrix [14] which describes the hole kinetic energy at the top of the valence band near **k**=0.

Baldereschi and Lipari [15] have used this Hamiltonian to calculate the energy levels of direct excitons in diamond and zincblende semiconductors. They first separate (2.9) into the sum of a diagonal Hamiltonian and a non-diagonal Hamiltonian. They obtain exact eigenstates and eigenvalues from the former, which can be reduced to the hydrogen-atom Hamiltonian and then treat the latter as a perturbation. The values obtained from their calculations will be compared with my experiments in the results section of this thesis.

In the absence of impurities or defects, the story of excitons would probably end here. The study of excitons has found an application mostly because of its high sensitivity to deviations from the perfect crystal, as will be discussed in the last section of this chapter. Semiconductors, as pure materials, are of little use. It is the fact that their electrical and optical properties can be drastically changed in a controlled fashion with the inclusion of impurities that has put them at the heart of modern technology.

Impurities

The only kind of impurity (or defect) that will be discussed here is a *point* defect which consists of a discrete atomic substitution. Such impurities have been identified in InAs by the work reported here. There are numerous other kinds of defects such as dislocations (line defects) or other point defects such as atomic vacancies, but the reader is referred to reference [17] for more information.

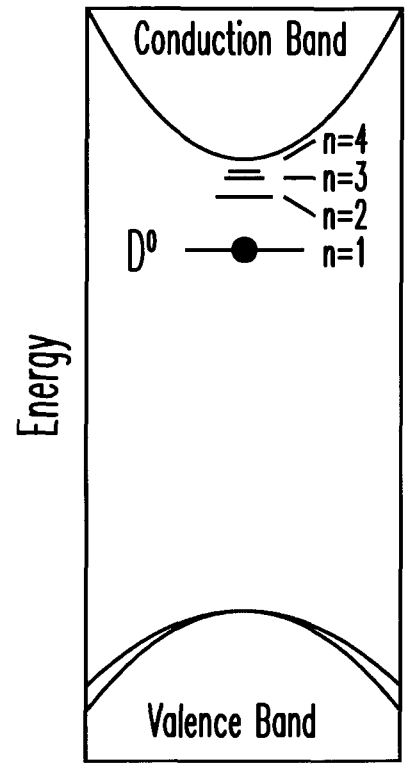

Figure 6. Quasi-hydrogenic levels of the neutral donor (D^0). The position of the electron represents the ground state of this system.

Within the impurity defect type, several subgroups exist. Foreign substitutionals with chemical valence less than that of the occupied site are called acceptors. If the valence is larger, the impurity is a donor. The isovalent (or isoelectronic) impurity consists of a substitution with an atom of the same column in the periodic table. An antisite defect, in AB compound semiconductors, is where an A atom occupies a B site or vice versa (this type must also be a double-acceptor or double-donor in a III/V semiconductor). Within these we shall only discuss charged impurities, which excludes isoelectronics.

Shallow donors

The easiest example of this type of impurity is a substitution with an atom that is one column to the right on the periodic table. An example in well-characterised semicon-

ductors is phosphorous in silicon. The phosphorous atom is pentavalent in a host lattice of atomic valence four. The extra electron is loosely bound to the impurity atom and can easily be thermally ionised, putting an electron in the conduction band and leaving a positively charged lattice site.

The eigenstate of the system is simply a scaled hydrogen atom, with the electron-at-infinity energy at the bottom of the conduction band. (Theoretically, the quasi-hydrogen model wavefunctions describe the envelope function to conduction band Bloch functions defined by equation (2.7).) The quasi-hydrogen levels of the shallow donor are shown schematically in Figure 6 superimposed on the band structure to show the relative energies. A ground state electron bound to the donor will have a binding energy given by the effective Rydberg

$$R_0 = \frac{m_e^* e^4}{2\hbar^2 \varepsilon^2}. \tag{2.10}$$

It will also have a spatial extent given by the effective Bohr radius

$$a_0 = \frac{\varepsilon \hbar^2}{m_e^* e^2}. \tag{2.11}$$

The above assumptions are valid for *shallow donor* states, where the binding energies are small with respect to the band gap.

Shallow acceptors

The hydrogenic effective mass theory just described for shallow donors can also be used for the acceptors, with the exception that as for the exciton, the more complex band structure of the hole must be used. The general picture nevertheless remains the same, as shown in Figure 7. An atom with valency one less than the occupied site has an extra hole, which can be thermally ionised to the valence band, leaving a negatively charged site.

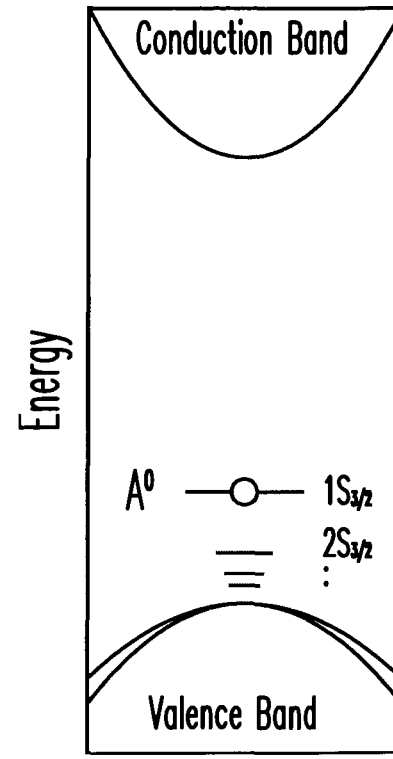

Figure 7. Neutral acceptor states showing a hole in the ground state $1S_{3/2}$, and schematic representations of the excited states, given in Table II.

Similar to the exciton, the Hamiltonian in its matrix form can be solved [16] by first finding the hydrogenic eigenstates of the diagonal part, then solving for the cubic contributions as a perturbation. The results are summarised in Table II.

Table II. Theoretical energy spectrum of acceptor impurities in InAs, from Baldereschi and Lipari [16]. The energy unit is meV.

$1S_{3/2}(\Gamma_8^+)$	$2S_{3/2}(\Gamma_8^+)$	$2P_{1/2}(\Gamma_6^-)$	$2P_{3/2}(\Gamma_8^-)$	$2P_{5/2}(\Gamma_8^-)$	$2P_{5/2}(\Gamma_7^-)$
16.31	5.00	0.420	7.91	4.76	3.63

Donor-acceptor-pairs

If both donor and acceptor impurities are present, the situation is quite different, in the sense that the neutral impurity is no longer the ground state for the electron or hole. The loosely bound extra electron of the donor, can now reduce its energy by migrating to the neutral acceptor site, where an electron is missing. This process is called *donor-acceptor-pair* recombination. The final ground state leaves both a negative and a positive charge in the lattice. The energy of this final state will depend on the distance between the charged donor and acceptor, since their Coulomb fields can cancel and reduce their total energy with respect to pairs that are infinitely apart (or neutral pairs). The resulting emission is therefore a broad band, rather than a sharp line in the spectrum. These levels are

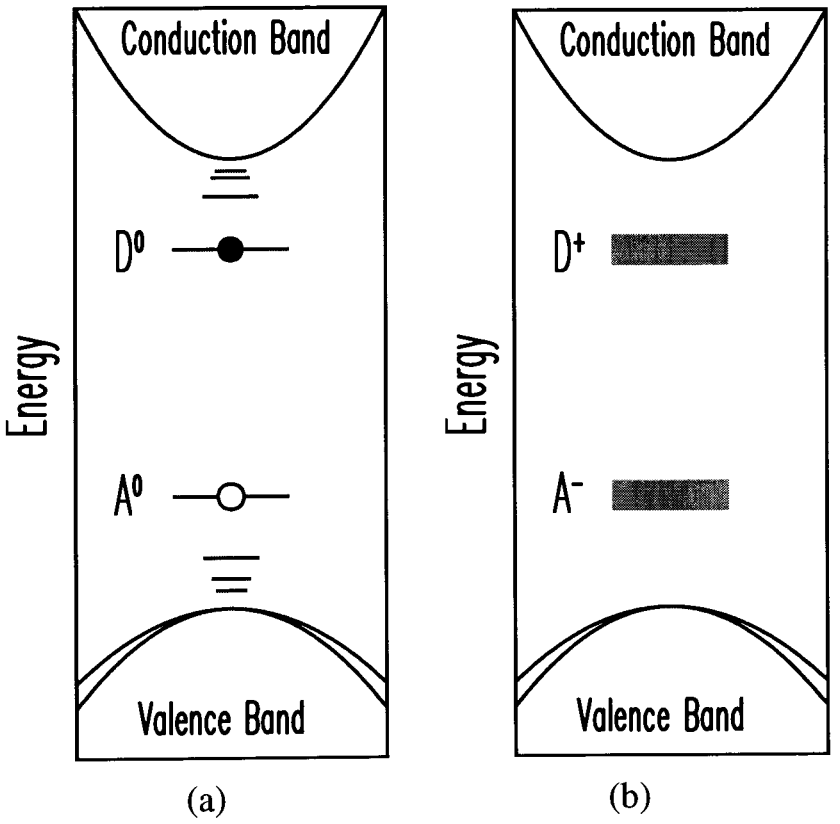

Figure 8. Donor-acceptor pair states. (a) Neutralised (excited) state. (b) Ionised ground state broadened by the Coulomb interaction between the ions.

shown in Figure 8. The *donor-acceptor-pair* (DAP) band shape and width will depend on the relative spatial distribution of excited pairs and this is one way of recognising this particular feature in the photoluminescence spectrum. This will be discussed in more detail in chapter four. In some semiconductors, a series of sharp lines are observed at the high energy edge of the DAP band. These correspond to very close pairs, and are a manifestation of the discrete nature of the inter-atomic distances.

The terminology for charged impurities in semiconductors is quite intuitive. If there is an equal amount of donor and acceptor charges, the material is said to be *compensated.* In that case, the electrical conductivity is poor, as that of a pure (intrinsic) semiconductor. If there is an excess of electrons or holes, the material is conducting, and is said to be *n-type* (negative) or *p-type* (positive) respectively. Intentional inclusion of impurities is called *doping*. A material which contains no intentional charged impurities is said to be *undoped,* although residual impurities are always present. The lowest concentration of impurities in InAs ever reported has been for the material studied for this work, and is approximately 2×10^{14} cm^{-3}. This is quite pure, considering the 10^{24} atoms per cm^3 in the crystal. But as the results will show, it is still a considerable concentration because of the enormous effective radius of electrons bound to neutral donors. As a result, free excitons that travel in the material cannot avoid being captured by defects.

Excitons Bound to Neutral Donors and Acceptors

Let us go back to the life of excitons now that the situation is more realistically described with the inclusion of impurities. The excitation used to produce electron-hole pairs will first populate the acceptor and donor sites. Initially ionised in their the ground state (Figure 8 (b)), the donors and acceptors will first be populated before free electrons and holes are, since this is the lowest energy configuration (Figure 8(a)). Only then can excitons be created.

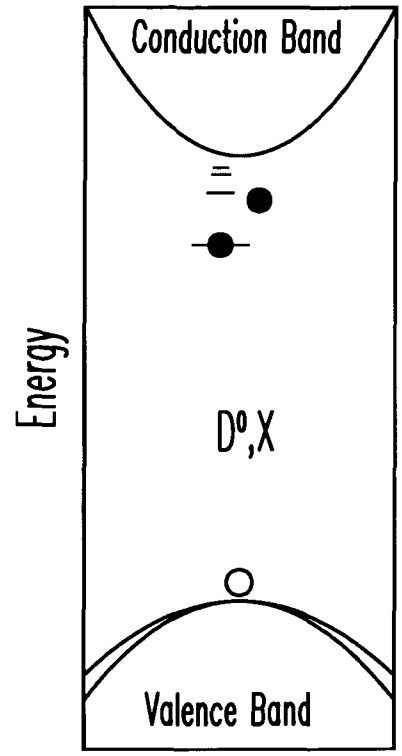

Figure 9. An exciton bound to a neutral donor (D^0,X). Its energy is reduced by the neutral-donor-bound exciton binding energy from that of the free exciton (X).

If an exciton (X) comes close enough to a neutral donor (D^0), a larger complex can be formed, now consisting of two electrons (one from the exciton and one from the neutral donor), a hole, and the positive impurity. This complex is called a *neutral-donor-bound exciton* (D^0,X), and its constituents are shown schematically (in reality, the two electrons cannot be distinguished) in Figure 9.

The same is true for an exciton that encounters a neutral acceptor. It can form a neutral-acceptor-bound exciton (A^0,X), a complex formed from two holes, an electron and the central negative impurity ion (shown schematically in Figure 10).

The binding energy associated with these complexes is or course larger than the binding energy of an exciton. The difference is called the A^0,X or D^0,X binding energy. It is smaller than, and related to the acceptor (E_{BA}) or donor (E_{BD}) binding energies by an empirical linear relationship known as Hayne's Rule (Haynes, 1960):

$$E_{BA}^{exc} = a + bE_{BA} \quad \text{or} \quad E_{BD}^{exc} = c + dE_{BD}. \tag{2.12}$$

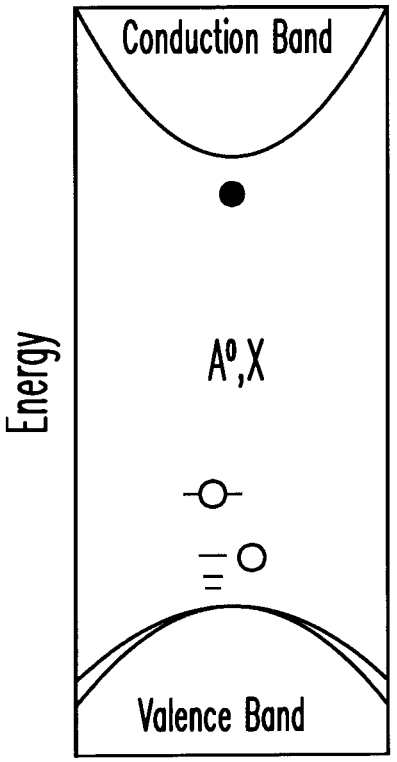

Figure 10. An exciton bound to a neutral acceptor (A^0,X).

Typically, the scaling constants b and d are of the order of a few tenths, meaning that the neutral-impurity-bound exciton binding energies are in the order of a few tenths of the acceptor or donor binding energies. In the framework of effective mass theory however, the binding energies should all be the same! Only the valence number is used in the calculations, and so all donors should have the same binding energies, and all acceptors alike. But the existence of *Hayne's Rule* implies that this is not the case.

Identification of Impurity Species

The properties related to the inner electron shells of atoms in the crystal, which are not considered at all in effective mass theory, are collectively referred to as *central cell effects.* In impurity-bound states, these effects become important when the wave functions are concentrated at the impurity centre. This means that some signature of the specific impurity is stored in the binding energy, and

therefore in the recombination energy which is carried by the emitted photon. This is why the measurement of impurity-bound exciton binding energies is a useful tool for characterisation. By identifying the position of photoluminescence lines as due to a specific impurity, the presence of that impurity is then signalled by the presence of that line in the photoluminescence spectrum. Because the low temperature photoluminescence of impurity-bound excitons can sometimes be measured for trace impurities as low as 10^{11} cm^{-3}, it is therefore a very useful tool for identifying contaminants in high purity semiconductor growth reactors.

THE TOTAL ENERGY PICTURE

In order to graphically describe the various exciton complexes, we have used schematic diagrams based on the band structure of indium-arsenide. This was done in order to gain insight on the formation of these objects, and also because it was a natural progression from the description of electrons in a crystal. As was pointed out however, those diagrams incorrectly describe other aspects of excitons, for example in Figure 9, where there seems to be two distinct electron states in the D^{O},X. In reality, the three-particle system consists of a hole and two electrons all bound to a positive ionic impurity. The electrons cannot be distinguished. Also, the photon emitted from the recombination of an electron and a hole, results from an initial to final state transition which cannot be depicted in Figure 9.

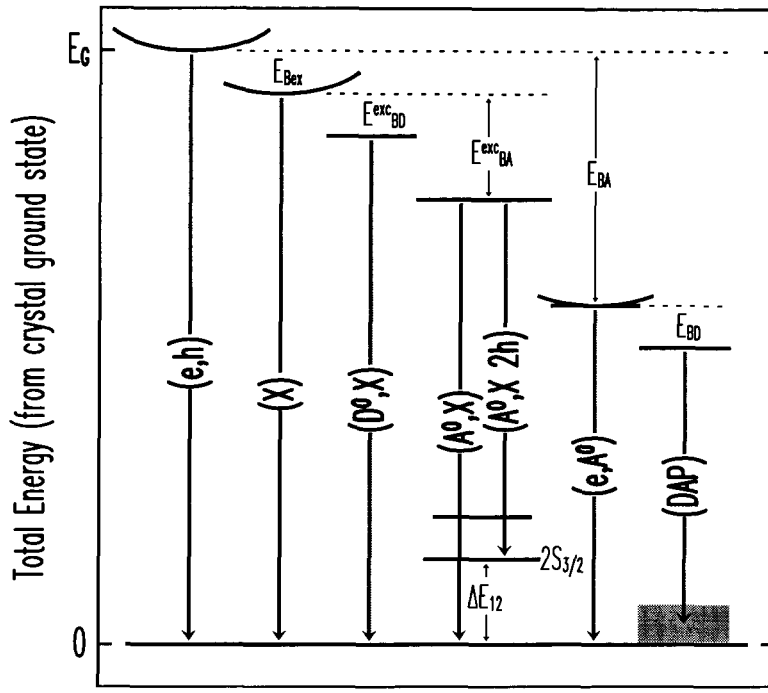

Figure 11. The total energy picture. The initial and final states of the photoluminescence processes identified in this work are shown . The zero of energy represents the ground state of the crystal. The binding energies involved in the reduction of the initial state energies are also given.

For that purpose, a diagram describing the total energy of the crystal, with initial and final states of photoluminescence processes experimentally identified in this work is given in Figure 11. (The abbreviations used in the figure are used throughout the thesis and a full list can be found on page ix.) The only transitions which are not explicitly described in the previous section are (A^O,X 2h) and (e,A^O). The former is the recombination of an exciton bound to a neutral acceptor whose final state is an excited state of the neutral acceptor (2h denotes the two hole processes involved. The transition leaving the acceptor in the ground state, (A^O,X), is called the principal transition). The latter (e,A^O) is the recombination of a conduction band electron with an acceptor-bound hole.

THE EFFECT OF AN EXTERNAL MAGNETIC FIELD

The conduction and valence bands, as well as excitonic and impurity-related states are affected by the presence of an external magnetic field. The most obvious consequence is certainly that the spin degeneracy is lifted, but other more complex dependencies are expected from such complicated systems. The magnitude of these effects not only scales with the magnitude of the field, but is also material dependent.

In InAs, because of the small effective mass of the electron, and hence the large spatial extent of its wave function, the high-field regime is reached at a relatively small magnetic field. This can be seen in the definition of the Bohr magneton $\mu_B = \hbar e / m_0$, which can be regarded as a magnetic energy unit for electrons. In the context of effective mass theory, one can expect that (ignoring spin), the mass of the electron can be replaced by the effective mass of the conduction band in semiconductors. Thus the effect of the magnetic field is enhanced by the ratio m_0 / m_e^*, which is ~40 in InAs.

CARRIER MOBILITY

The carrier mobility of a material is a standard measure of its purity. It essentially measures how far a carrier can travel before being scattered. Any imperfection in the crystal including phonons, dislocations, impurities (neutral or ionised) contributes to the scattering. This is different from the conductivity, which is mainly governed by the number of carriers present. All things being equal, a higher mobility results in a faster signal transmitted by the carriers, since they travel unimpeded through larger distances. The in-

trinsic mobility of semiconductors is governed by external factors, such as temperature and applied field, as well as intrinsic properties such as the carrier effective masses. Theoretically, the mobility is inversely proportional to the effective mass, and proportional to a relaxation time (although this relaxation time usually also depends on the effective mass).

CHAPTER 3 - EXPERIMENTAL TECHNIQUES

This section describes the techniques of growth and characterisation used to obtain the results presented in this thesis. A general description of the epitaxial growth method is given first, then the experimental aspects of semiconductor photoluminescence measurements using Fourier transform spectroscopy are described. Also, the various techniques specific to measurements in the mid-infrared are discussed with particular emphasis on the two methods used, namely cold-filtering and the use of a cryogenic Fourier transform interferometer.

GROWTH TECHNIQUE - MOCVD

All the spectroscopy reported in this thesis was performed on InAs material prepared using "metalorganic chemical vapour deposition". In this method, the indium and arsenic atoms are initially attached to organic radicals, making the source material less-reactive. For this work, the InAs epilayers were grown using tertiarybutylarsine (TBA) and trimethylindium (TMI) as the "metal organic" sources. The attached organic radicals may be very complex but they play a neutral role in the final steps of the growth process as will be described shortly.

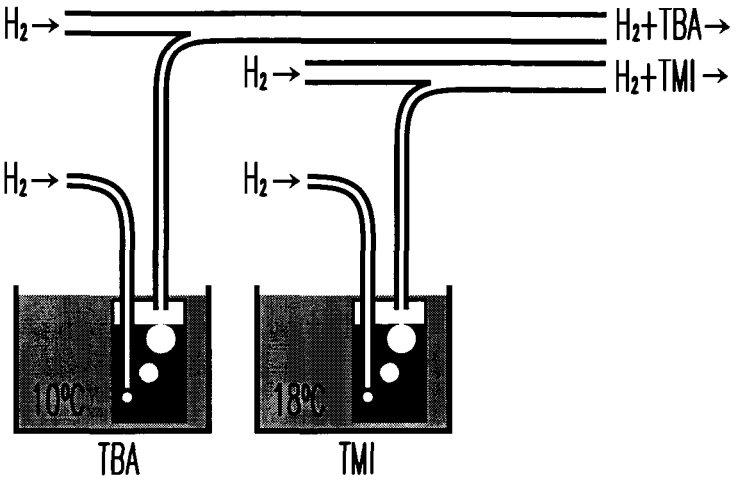

Figure 12. Schematic of the hydrogen "bubblers" used to contain and transport the metal-organic sources to the reactor.

The source chemicals used in MOCVD can be either in the form of a liquid (as is the case of TBA) or a solid (TMI). They are maintained at a fixed temperature in liquid baths as shown in Figure 12. During growth, hydrogen gas (H_2) is forced to the bottom of the source (much like blowing through a straw in a glass of milk) so that bubbles float to the top with a saturated vapour pressure of the source chemical. The chemicals are then carried by the hydrogen flow to the reactor chamber. Before these gases reach the reactor, they are merged with a "carrier flow" of hydrogen which is automatically adjusted to maintain a constant total flow at the reactor whether the sources are turned on or off. This is done in order to avoid turbulence. In the SFU MOCVD reactor, the total flow of hydrogen entering the reactor was typically ~2.3 standard litres per minute, at a reduced pressure of 50 torr.

Once the "metalorganic" gases reach the reactor, they enter the mixing chamber at the top and flow downwards through a quartz tube. Surrounding the quartz tube, yet another flow of hydrogen is used to create a laminar cylinder of gas inside which the source-

containing column of gas will reach the horizontal growth surface. This is shown schematically in Figure 13 with arrows showing the flow lines. The larger-tipped arrows depict the hydrogen gas cylinder inside which flows the mixture (smaller-tipped arrows) of TBA, TMI and carrier hydrogen. The actual inside diameter of the growth chamber is 6.2 cm and the sample diameter can be up to 2.5 cm.

The sample substrate rests horizontally on a heated carbon susceptor, as shown in the lower centre of the chamber in the figure. The hot boundary layer of gas just above the sample is where all of the steps for epitaxial growth occur. This is where the "metal organic" gas decomposes into the molecular constituents of the crystal. The exact breakdown sequence of the molecules is very complicated and is still a subject of debate. However, the purpose of the organic radicals is to carry the chemicals from the source to the boundary layer. There, they either fully or partially dissociate from the indium and arsenic as those are deposited on the

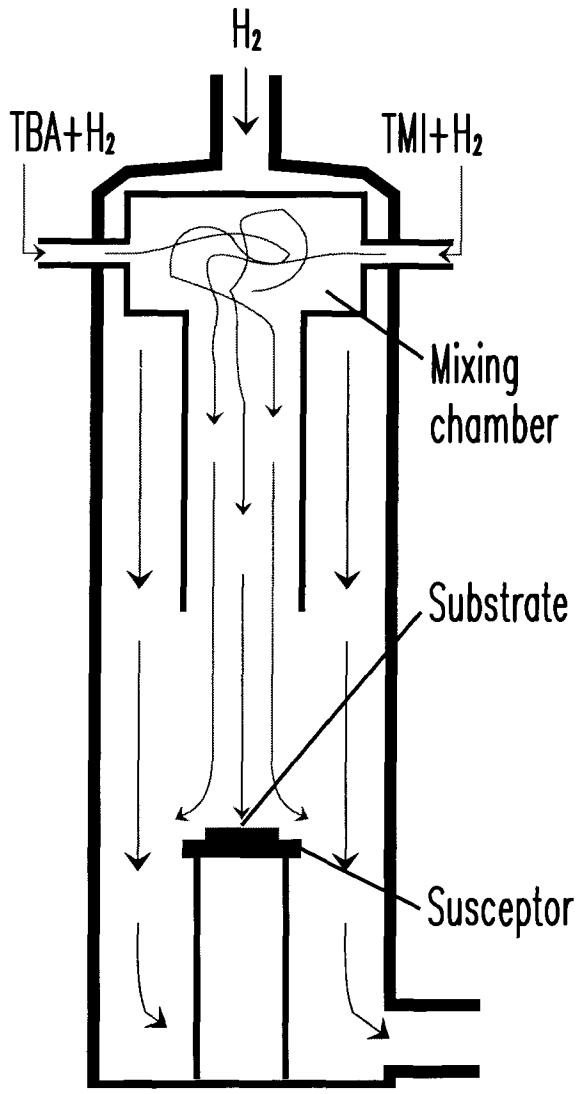

Figure 13. Schematic of the MOCVD reactor chamber showing the gas flows and the position of the sample susceptor.

semiconductor surface, and play no important role beyond that stage.

The details of how the indium and arsenic travel on the surface to form the crystal is again beyond the scope of this work. For InAs, as well as any other III/V material, the preferred atomic configuration (below the surface) is governed by ionic binding. The resulting crystal structure for InAs is zincblende, like that of GaAs and InP.

GROWTH OF INAS FOR PHOTOLUMINESCENCE STUDIES

In order to obtain good optical properties in semiconductors, the number of non-radiative traps such as dislocations and defects must be minimised. If the substrate material on which the epitaxial growth is performed is not the same as the deposited material, there will normally be a lattice size mismatch. Here lies the art behind the science of epitaxial growth. If the lattice mismatch is large, the creation of dislocations at the interface is unavoidable. One solution is to sacrifice the first part of the growth as a buffer layer, to absorb and "smooth out" the dislocations. The buffer layer is grown at a lower temperature in order stop the propagation of interface dislocations. Because this layer relaxes to the lattice of the intrinsic deposition material, it is referred to as a *relaxed buffer layer.* The new surface is then lattice-matched to the deposition material and epitaxial growth can be performed, in principle, on a dislocation-free surface.

The "relaxed buffer layer" method just described was used by Dr. Simon Watkins' group to grow InAs on GaAs semi-insulating substrates. However, the resulting material was not well suited for optical characterisation as the residual dislocation density (typically 10^7 cm^{-2}) was still too large and the intrinsic optical properties of the material were lost to

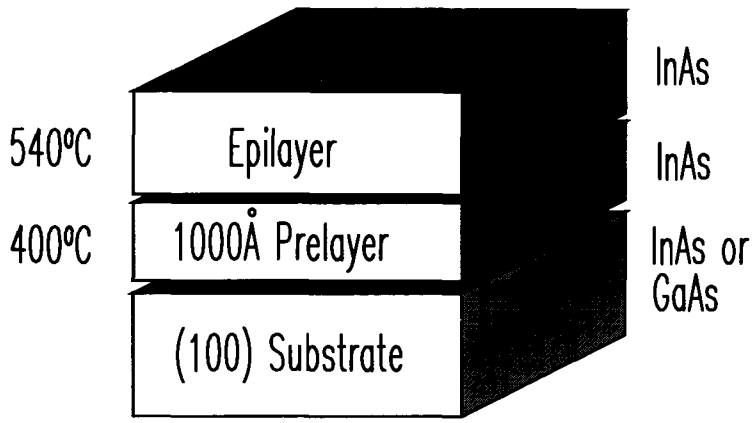

Figure 14. Relaxed buffer layer growth profile.

inhomogeneity effects (see Figure 29). InAs samples grown on InAs cannot be used for electrical characterisation because the epilayer properties are masked by the properties of the more conducting substrate. Figure 14 shows the schematic arrangement of the InAs epilayers with typical growth temperatures and thicknesses. To ensure that the same material was optically and electrically characterised, simultaneous growth on both substrates was performed.

The samples prepared for photoluminescence studies were grown on undoped liquid encapsulated Czochralski, nominally exact (100) InAs substrates, with residual n-type carrier concentrations of approximately 2×10^{16} cm^{-3}. The epitaxial material was residually n-type with donor concentrations as low as 2.5×10^{14} cm^{-3} and mobilities of up to 1.2×10^{5} cm^2/Vs. These measurements were made by Dr. Watkins' group. A more detailed description of the growth methods as well as transport characterisation data were reported in reference [20]. The optical characterisation method is described next.

LOW TEMPERATURE PHOTOLUMINESCENCE SETUP

As described in chapter 2, photoluminescence is the emission of light resulting from optical excitation of the medium. For semiconductor studies, the only requirement

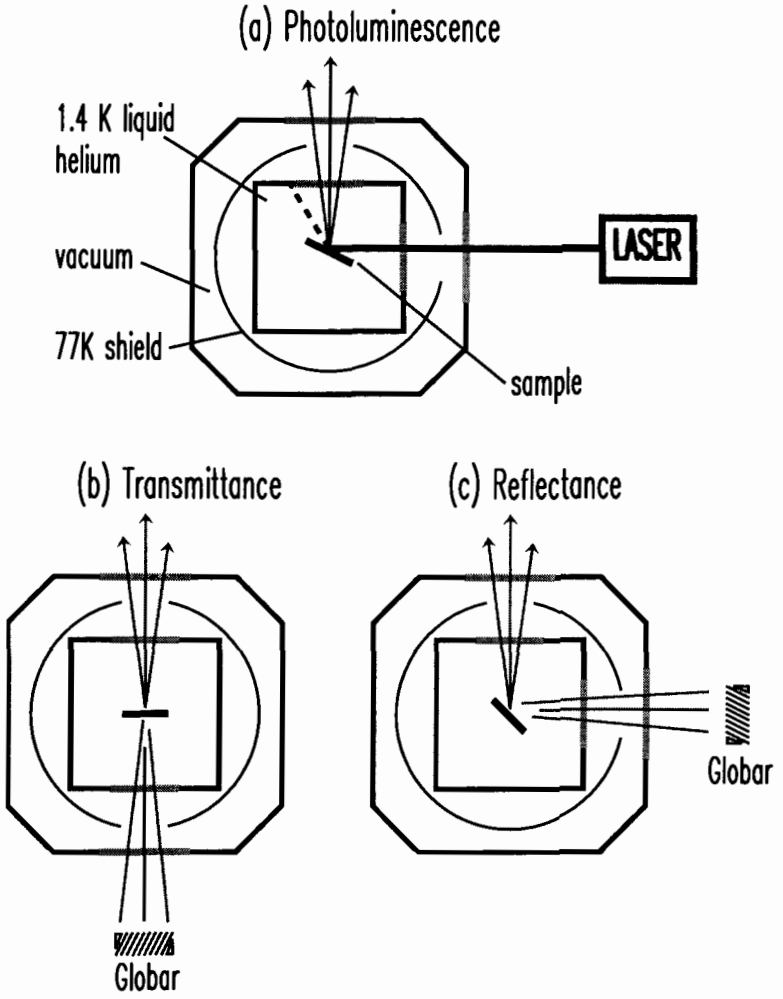

Figure 15. Top view of the sample chamber in the liquid helium cryostat, showing the different configurations for photoluminescence, transmittance and reflectance measurements. A Globar is essentially a heated element with broad blackbody emission in the infrared.

on the optical excitation is that the photon energy be larger than the forbidden band gap between the electron and hole states in the semiconductor, in order to create the electron-hole pairs. The excitation source used in this study was emission from an argon ion laser, which has its main lines in the blue and green, much higher than the minimum energy requirement.

In order to study exciton processes, the semiconductor sample must be kept at a temperature lower than that required to dissociate the exciton complex. For InAs, it will

be shown that this temperature is much lower than the atmospheric pressure liquid helium temperature of 4.2 Kelvin. Therefore most of the measurements were performed with the sample immersed in superfluid liquid helium with a temperature of ~1.4 Kelvin. To achieve this temperature, a large-volume vacuum pump is used to continuously remove the helium vapour above the liquid, so that a reduced vapour pressure is established. The latent heat of evaporation continuously removed from the liquid in an attempt to reach equilibrium is the source of the cooling mechanism.

The top-view geometric configuration of the photoluminescence setup is shown in Figure 15(a). For transmission and reflectivity measurements, a broad Globar source (a heated element) was used and the different configurations are shown in Figure 15(b) and Figure 15(c) respectively. Transmission measurements were possible because of the transparency of the substrate material in the band-edge region, due to the Burstein-Moss effect. (This transparency is caused by the filling of the bottom of the conduction band from extrinsic electrons, which raises the lowest available electron state.) For measurements under magnetic field, the samples were immersed in a split-coil horizontal superconducting magnet dewar capable of fields up to 7 Tesla. For the results reported here the sample's principal orientations were not aligned with the magnetic field.

FOURIER TRANSFORM SPECTROSCOPY

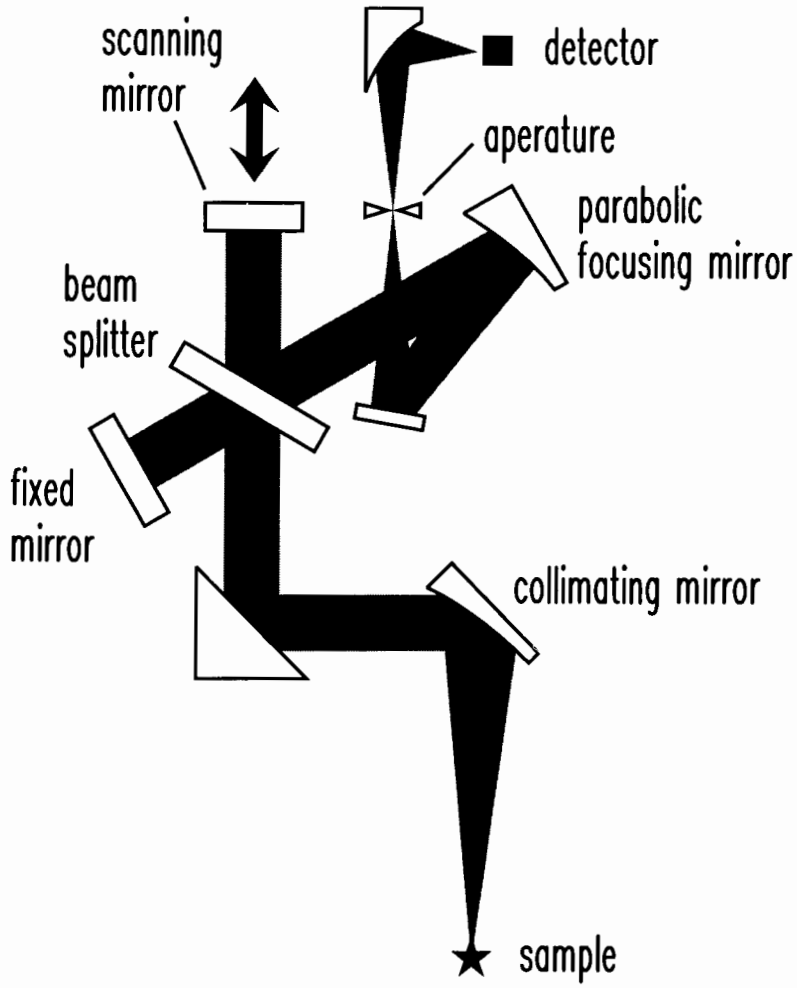

Figure 16. Components of a Fourier Transform spectrometer and the optical path.

The method of Fourier transform spectroscopy (FTS) was used to measure the optical spectrum of InAs. Unlike the more conventional method of dispersive spectroscopy (DS), where the light intensity is measured directly as a function of energy, here the interference of the emitted light with itself is measured as a function of phase difference (called an interferogram). By taking the Fourier transform of the interferogram, we then obtain the light intensity as a function of energy, without any loss of information. In fact, for many applications, FTS has several advantages over DS and the reader is referred to

reference [18] for details on this matter. For measuring high resolution spectra over a large range of photon energies, simply on the basis of practicality, FTS is the method of choice.

As shown in Figure 16, the central piece of the optical schematic is a beam splitter, arranged to separate a beam of collimated (parallel) light. The luminescence originating from the sample (a star in the figure) is first collimated, then half of it is reflected by the beam splitter to a fixed mirror, while the other half continues to a scanning mirror. The light from both mirrors returns by the same path to the beam splitter. After passing the beam splitter again, the light beam is the sum of two identical plane waves that have travelled different distances. Thus the two waves interfere with each other. As the figure shows, half of this interference plane wave goes on to be focused by a parabolic mirror, through a spatial filter, and is refocused at the detector. The other half, going back toward the sample, is lost.

As the position of the scanning mirror is changed, so is the path difference and hence the interference condition. This intensity change, measured by the detector as a function of path difference, is called an interferogram.

The spectrum, (intensity as a function of photon energy, wavelength or frequency), is obtained from the *Fourier transform* of the interferogram. To understand why this is so, one simply has to realise that the interferogram is actually the *inverse Fourier transform* of the spectrum of the measured radiation. Imagine a monochromatic light source of wavelength λ (or of photon energy $(1/\lambda)$ in units of wavenumbers). If the interferometer

path difference is $d=n\lambda$, the light waves will add constructively at the detector. For $d=(n+1/2)\lambda$, they cancel. The resulting interferogram $I(d)$ is a cosine wave with period λ. The operation just described, which transforms the frequency domain into the spatial domain, is called an *inverse Fourier transform.*

These properties are common to all FTS systems, although the specific geometry may vary. The spectra presented in this thesis were measured with a Bomem DA-8™ Fourier transform spectrometer using a cold band-pass filter against the detector, as well as a Bomem DA-3™ modified for mid-infrared measurements, which are the subject of the next section. In order to calculate the spectrum, these instruments use a high-quality analog-to-digital converter to store the interference change measured by the detector as a function of path difference. A dedicated vector processing board is used to perform the mathematical manipulations on the interferogram in order to minimise the time required to obtain the spectral information. A host computer is used to retrieve the information from the vector processor as well as to send commands and receive status information from the interferometer.

MID-INFRARED TECHNIQUES

One can qualitatively define the mid-infrared as the energy region from a few hundred wavenumbers (cm^{-1}) to a few thousand. This is also where the bulk of the room-temperature blackbody radiation is emitted. The higher energy region where there is negligible blackbody radiation, below the visible region, is loosely called the near-infrared. The energy region from near zero to a few hundred wavenumbers is referred to as the far-

infrared. Most conventional semiconductors, such as Si, Ge, GaAs and InP have a band gap in the near-infrared. Narrow-gap semiconductors, such as InSb and InAs, have their band gap in the mid-infrared, where the room temperature blackbody radiation striking the detector, including that emitted from the instrument's optical components, can be hundreds of times greater than the photoluminescence intensity being measured. This is where one of the advantages of Fourier transform spectroscopy, that the detector measures the entire spectrum at all times, becomes a clear disadvantage.

Unlike dispersive spectroscopy, there is no intrinsic light rejection to select the region of interest. Because the detector noise is proportional to the square root of the total integrated signal measured (at zero path difference), FTS must make use of filters to block spectral regions that may be much brighter than the region of interest in order to increase the signal-to-noise ratio. In the case of blackbody radiation, this poses a problem since the filter itself can be a source of radiation.

Several techniques exist to enable measurement in the mid-infrared region. One of them involves the modulation of the input luminescence and consequent deconvolution of the signal using lock-in techniques to separate the sample luminescence from the background radiation. However, this method does not solve the detector sensitivity problem and hence does not improve the signal to noise ratio.

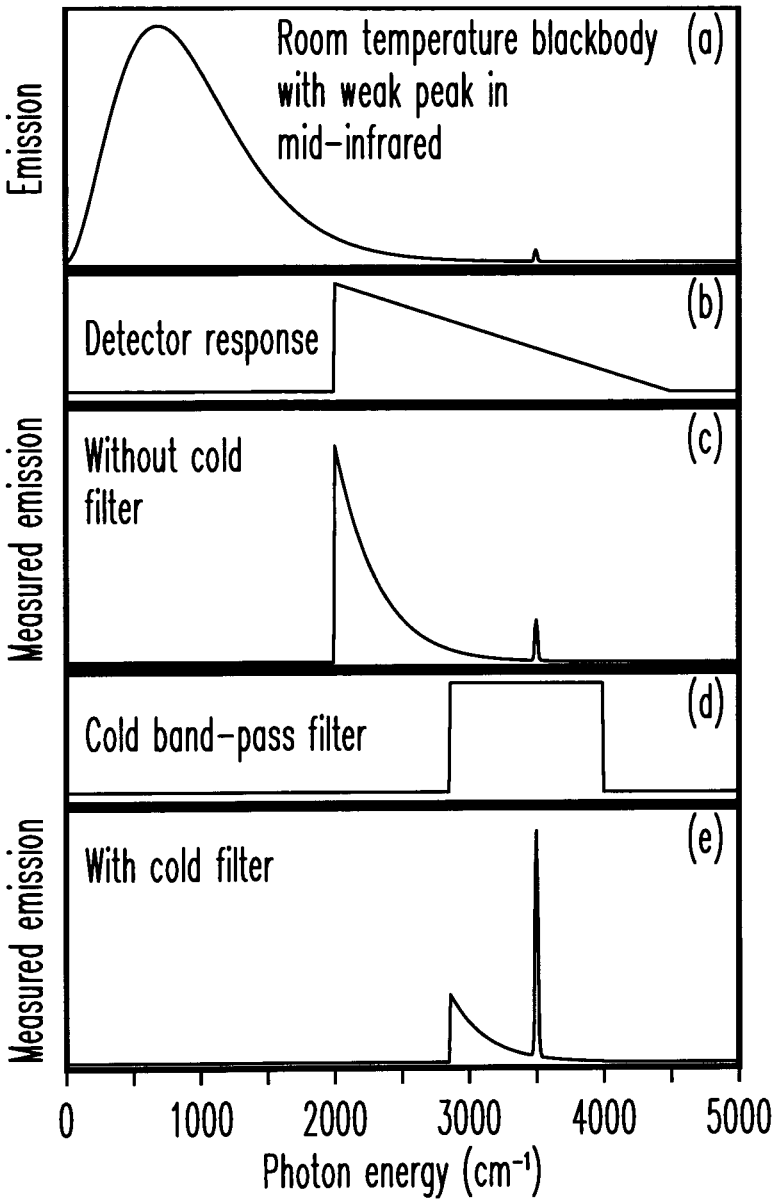

Figure 17. Cold filter method. (c) is the result of the detector response (b) on the spectrum (a). A further improvement in signal-to-background is obtained in (e) with the use of a cold band-pass filter schematically shown in (d), between 2.5 and 3.5 μm. The units of energy used in this plot and also in the appendix, cm^{-1}, are called *wavenumbers* (1/wavelength in cm).

Cold Filter Method

As was just described, to block unwanted radiation, a band-pass filter is required in FTS to reduce the noise proportional to the square root of the total integrated intensity of

the spectrum. The detector itself is to some extent such a filter, since it is not sensitive to radiation below its intrinsic band gap, and becomes gradually insensitive at higher energies. An InSb photo-detector, cooled to 77 Kelvin has a response shown schematically in Figure 17(b). In part (a) of the figure, Plank's function for blackbody radiation at 300 Kelvin is plotted and a small artificial peak has been added near the band-gap of InAs form demonstration purposes. One can see from Figure 17(c) that the signal-to-background is increased by the detector response alone. Part (d) of the figure shows the response of an ideal band-pass filter between 2.5 and 3.5μm that has been cooled so that one may neglect its blackbody radiation. The result of using such a filter is shown in the bottom plot of Figure 17, where a dramatic increase in the signal-to-background ratio is seen.

This is the method that was used to perform most of the spectroscopy reported in this work. One can see that this method will work as long as most of the background radiation intensity is not in the region of interest. If for example the peak in Figure 17(a) had been near 1000 cm^{-1}, the cold-filter method would not have made a significant difference in the background reduction (and hence to the noise reduction). For such a situation, the solution is to remove the blackbody radiation which is seen by the detector by cooling all parts of the system between the sample and the detector.

Cryogenic Fourier Transform Interferometer

A significant effort was invested in the design, construction and operation of a FTS system that would have all the advantages of the Bomem DA-8™, as well as being able to measure emission in the mid-infrared, an energy region scarcely studied in semiconductors

because of the difficulties discussed above. Although the cold-filter method was sufficient to study much of the photoluminescence spectrum of InAs, it was not possible to know what lay beyond the cut-off of the filter (at wavelengths longer than 3.5μm) until the cryogenic Fourier transform interferometer project was completed. This did not occur until much of the work presented here had been done, so that only the deepest (lowest energy) photoluminescence features were measured using the cryogenic instrument.

It has been hinted throughout this chapter that a solution to the blackbody radia-

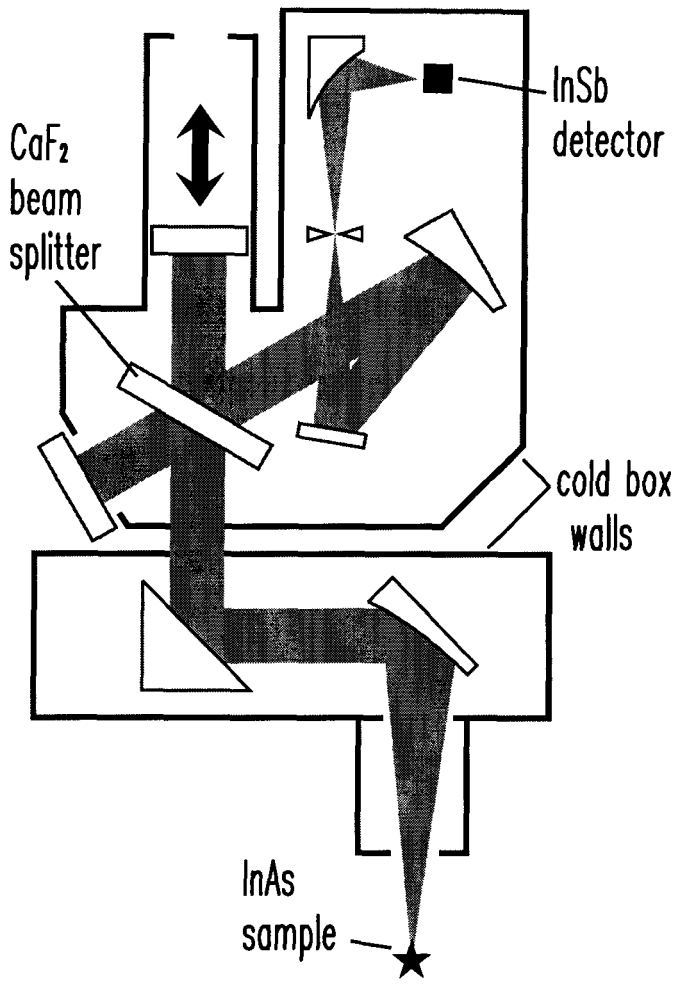

Figure 18. The optical path with cold components. The back, front and sides of the outlined box are cold. The only warm component is the fixed mirror, shown outside of the box. The scanning mirror is only radiatively cooled.

tion background problem should be to simply remove the radiation. This can be achieved by cooling the measuring instrument to a temperature low enough that the blackbody radiation is negligible in the detector response region. On the scale of Figure 17(a), the 77 Kelvin (liquid nitrogen temperature) blackbody curve is effectively a flat line at zero intensity. In reality it peaks at about 150 cm^{-1} and decays more or less exponentially at higher energy so that at the low energy end of the detector response, it is considerably reduced with respect to the room temperature emission. This is of course the theoretical limit, but it describes the intended goal, namely to operate a Bomem DA-3™ Fourier transform interferometer (the ancestor of the DA-8™ model) at a reduced temperature, by cooling its components with liquid nitrogen.

Figure 18 shows schematically the same optical configuration as that of Figure 16, now showing the walls of a cold box in which all the components are mounted and in thermal contact. Only the "fixed mirror" is kept warm and the scanning mirror is cooled only radiatively. The reason the fixed mirror is kept warm is one of design. Its angle is carefully controlled as part of a dynamic alignment feed-back loop, and it must be free to move. The front surface of the mirror, by definition, must have a very low emissivity and it was assumed that the effect of one warm mirror in the system would be acceptable. The results obtained confirmed that fact, but also showed that this mirror is the source of much of the residual blackbody radiation seen by the detector. At the time of this writing, work is in progress to cool this mirror also.

The scanning mirror is surrounded by a cold copper sleeve throughout its travel and is attached to the scanning mechanism with a 30 cm long thin-walled stainless steel

tube. From simple thermal diffusion calculations, in this configuration the scanning mirror should reach an equilibrium temperature of ~125 Kelvin if the back surface is exposed to 77 Kelvin radiation. The beam splitter as well as all the windows used for these experiment are made of CaF_2, which is transparent from the near infrared down to about 1000 cm^{-1} (10 μm).

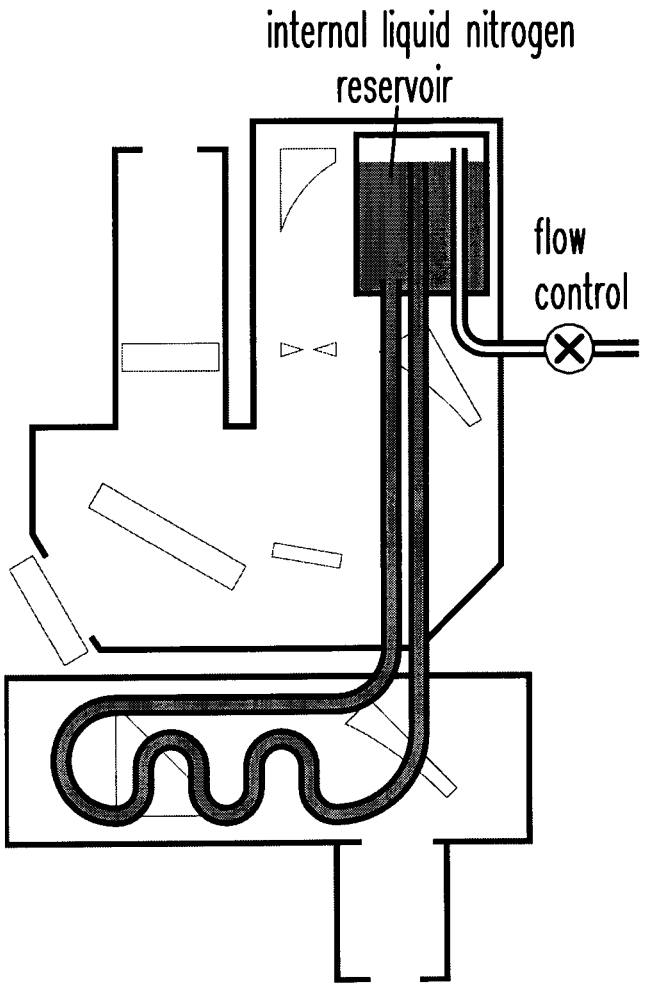

Figure 19. The liquid nitrogen cooling system consists of an external reservoir (not shown) which keeps the internal reservoir filled. A flow control valve is used to remove the evaporated nitrogen faster to increase the flow into the internal reservoir. The bottom part of the interferometer is cooled by a flow through a gravity-fed copper tube, as shown. The top part is cooled by contact with the internal reservoir.

The cold box as well as the mountings for the optical components are made of aluminium. The cooling medium is 77 Kelvin liquid nitrogen flowing through copper tubes from a copper reservoir which are in good thermal contact with the cold box. Some extra thermal links are added to weakly attached components via copper braids directly from the components to the liquid nitrogen reservoirs. The detector itself is mounted on a copper bridge extending from the top internal reservoir. Because the cold box is in fact two separate thermally linked boxes as shown in Figure 19, the copper reservoir is the main cooling source for the top interferometer box, while the flowing liquid nitrogen tubes mainly cool the bottom collimator box.

The entire assembly is itself fitted inside the more or less original casing of the Bomem DA-3™ interferometer from which all of the control electronics and some of the components were taken. This outer box is made to support a vacuum close to 10^{-5} torr at room temperature. The links from the cold boxes to the outer vacuum box are thin-walled stainless steel tubes. The average temperature achieved inside the cryogenic interferometer is about 100 Kelvin, and requires about 25 litres of liquid nitrogen per day to remain cold.

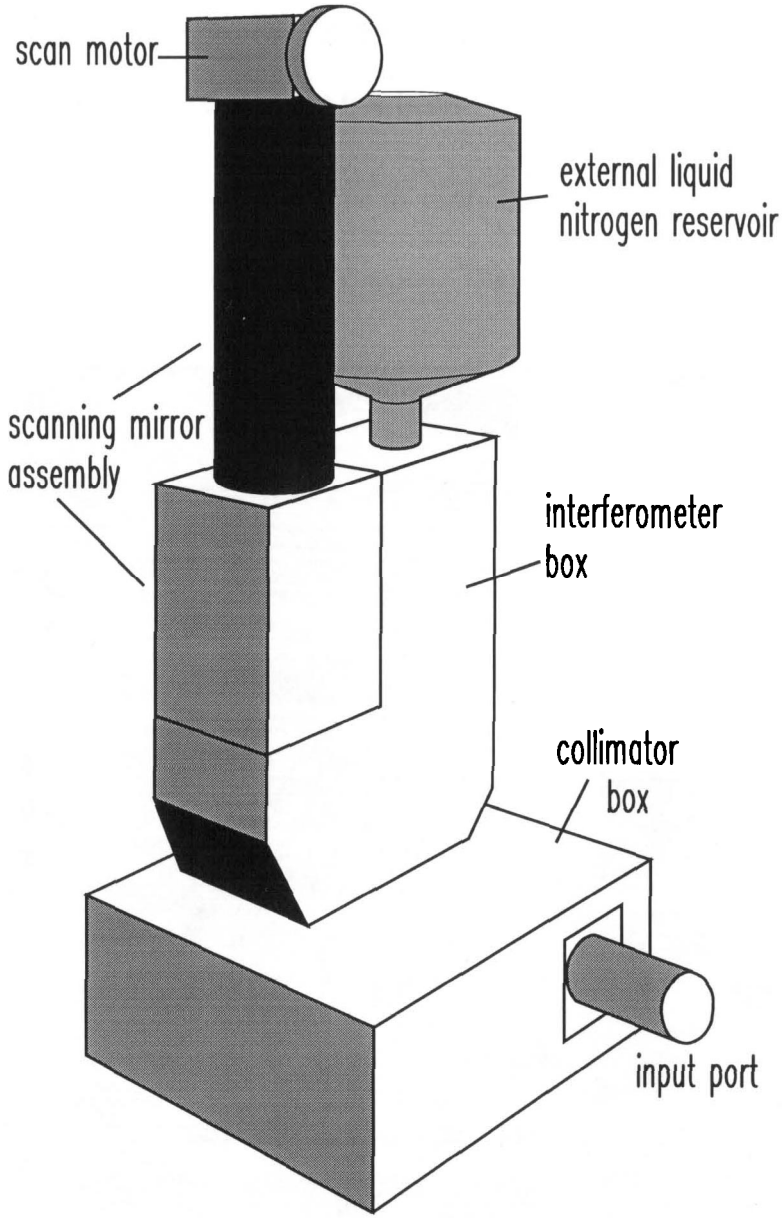

Figure 20. Perspective diagrammatic view of the cryogenic interferometer overall assembly.

In Figure 20, a perspective view of the interferometer assembly is shown, and a picture of the actual machine is shown in Figure 21. An obvious addition to the original design is the outer liquid nitrogen reservoir situated on top, which continuously fills the inner reservoir shown in Figure 19. Also shown in Figure 19 is a valve to control the exhaust of gaseous nitrogen from the inner reservoir. This valve can be adjusted to increase

the flow of liquid nitrogen in the cooling system, to compensate for the larger boiling rate during the initial cooling period of about five hours.

Some spectroscopy tests were done to verify that the interferometer had not compromised its performance in becoming cryogenic. These can be found in Appendix B.

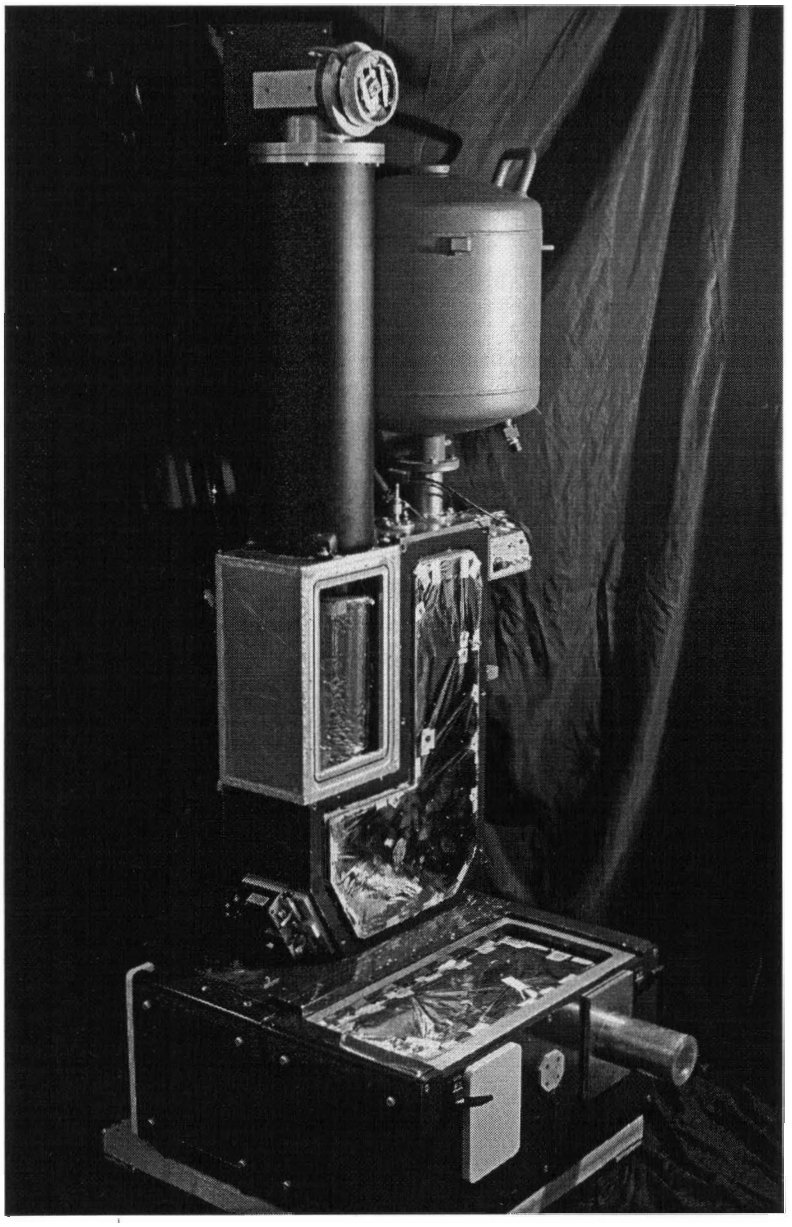

Figure 21. Picture of the cryogenic interferometer with the outer vacuum box open, showing the cold box wrapped in shiny insulating sheets.

CHAPTER 4 - THE SPECTRUM OF INAS

After a brief introduction to the exotic concept of excitons in semiconductors, and a description of the means and methods to observe them, it is time to show the evidence. This chapter is devoted to the identification of all the features observed in the photoluminescence spectrum of InAs at low temperature and zero magnetic field. In order to provide more insight on the nature of the observed peaks and to support the identifications, measurements were also performed under magnetic field, and at higher temperature, but no thorough examination of these dependencies was undertaken. As well, as described in the previous chapter, transmittance and reflectance measurements were performed to complement the photoluminescence information.

A very systematic approach is used in order to report, qualify and in some cases quantify the results obtained from the photoluminescence measurements. To reiterate, the goal is to correctly identify the mechanisms responsible for the specific peaks or lines or features of the spectra so that we can further our knowledge of the properties of InAs, specifically regarding impurity content. For other scientists to make use of these results, the findings are summarised in two tables, included in this chapter.

The chapter is divided primarily by spectral energy region, and subdivided by type of recombination. The low temperature photoluminescence spectrum of InAs may be

separated into three energy regions. The deepest, below 390 meV, contains a broad luminescence band from an unknown process as well as the phonon assisted transitions of the band edge luminescence. The middle energy region, between 390 meV and 402 meV, contains luminescence from DAP bands and the two-hole replicas of the A^0,X transitions. The excitonic region, in the energy range 410 meV to 416 meV, contains features corresponding to free exciton (polariton) recombination and impurity-bound exciton recombination. We first discuss the photoluminescence related to the acceptor impurities since this dominates the entire spectrum. Secondly, the other excitonic processes (free and donor-bound) are carefully examined, and we conclude with a discussion on the broad luminescent bands observed by us and other groups.

DONOR-ACCEPTOR PAIR BANDS

The spectra of Figure 22 span both the middle energy region and the excitonic region. Evidence for three different acceptor species A_1, A_2 and A_3 is clear from the three distinct donor-acceptor pair bands DA_1P, DA_2P and DA_3P. The luminescence origin of the DAP band is the recombination of a donor-bound electron with an acceptor-bound hole perturbed by the final-state Coulomb energy which depends on their relative separation r (see Figure 8 on page 21). Hence the emitted photon energy is given by

$$E_{DAP}(r) = E_G - E_{BA} - E_{BD} + \frac{e^2}{\varepsilon r} \tag{4.1}$$

where E_G is the InAs band gap at 1.4 Kelvin and E_{BA} and E_{BD} are the acceptor and donor binding energies. With increased excitation density, the distribution increases towards closer pairs so that the band shifts to higher energy and becomes broader.

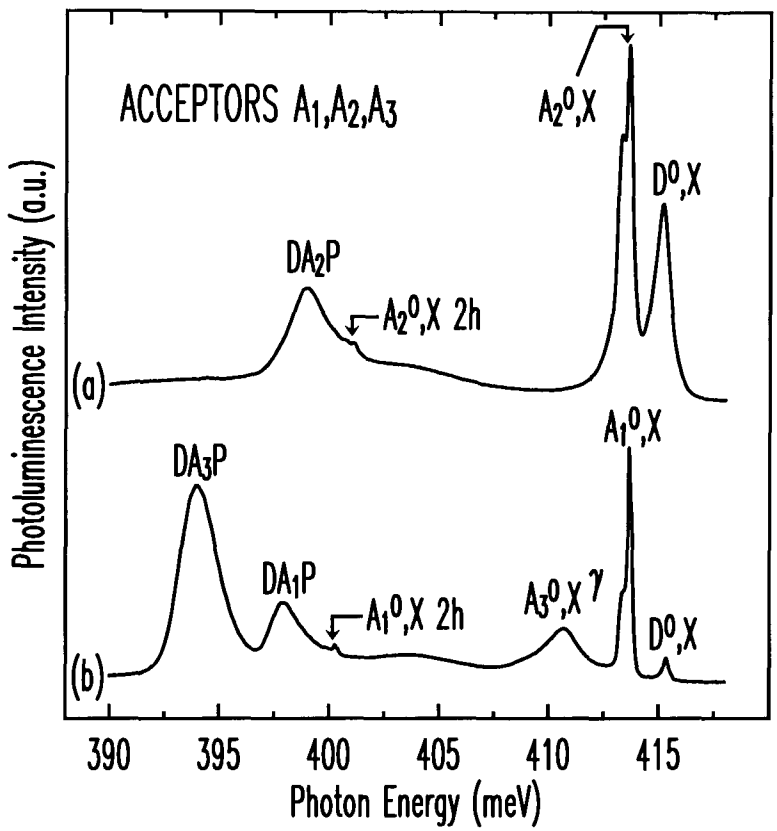

Figure 22. The photoluminescence spectrum of InAs at 1.4 K for an excitation power of 1 mW, showing the different acceptor features. (a) Sample containing one acceptor, A_2. (b) Sample containing two acceptors, A_1 and A_3. The neutral-donor-bound exciton (D^OX) is also shown.

The excitation density dependence of the sample of Figure 22(b) is shown in Figure 23 for excitation powers of 0.1, 1 and 10 mW/cm^2. Sub-figures (a) and (b) show the DAP bands for acceptors A_3 and A_1 respectively, with the higher energy curves corresponding to the higher excitation. The curves are scaled vertically to emphasise the blue-shift and broadening. The integrated photoluminescence intensities for the DA_1P bands of (b) is plotted on a log-log scale as a function of excitation power in Figure 23(c), along

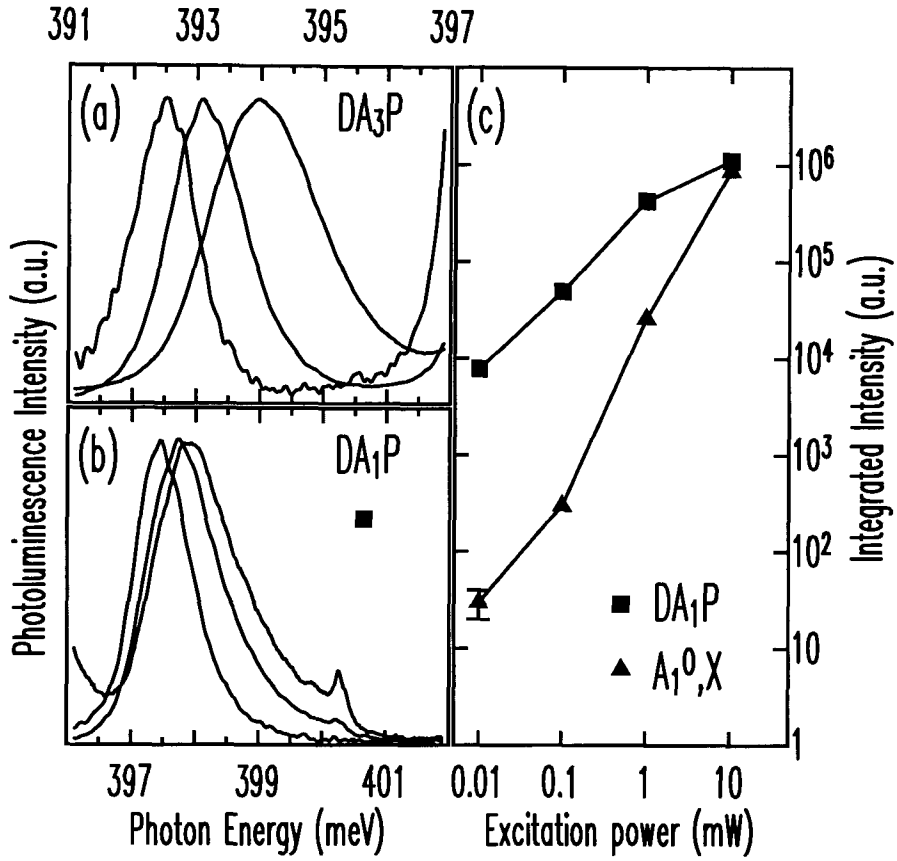

Figure 23. The excitation power dependence of the transitions shown in Figure 22(b). The blue-shift and broadening of the DAP band is shown for the acceptor A_3 in (a), and for A_1 in (b). The broadest and most blue-shifted curves correspond to an excitation density of 10 mW/cm^2 in the series 0.1, 1 and 10 mW/cm^2. The curves are scaled vertically to equal intensities. The integrated photoluminescence intensity as a function of excitation power for the DA_1P band is shown in (c).

with the corresponding A_1^O,X dependence. The bound exciton lines do not shift in energy with changing excitation density.

The power dependence is consistent with the two competing processes. As the DAP recombination begins to saturate (with the depleting number of ionised acceptors), the A^O,X start recombining on the neutral sites. The A^O,X recombinations increase super-linearly until they become the dominating process, and the DAP recombinations become

independant of excitation. Beyond that (not seen in the figure), the A^O,X dependence will become linear until the number of available neutral acceptors start to saturate.

The sub-linear dependence of the DA_1P band implies a saturation of this process, as expected from the above arguments. A similar power dependence is expected for the DA_3P band but is not observed up to 10 mW/cm^2. Because in all respects this feature behaves like a DAP band at these excitation densities, it is suspected that this sample contained more of the A_3 acceptors than the A_1 acceptors, and that DA_3P integrated intensity should saturate at a higher excitation. Another possibility for the difference in saturation behaviour is that the DA_1P pairs may have a much longer recombination time that the DA_3P.

ACCEPTOR-BOUND EXCITONS

Acceptors A_1 and A_2

In the excitonic region of Figure 22 are lines corresponding to the recombination of excitons bound to neutral acceptors (A^O,X). For the A_1 and A_2 acceptors, identical doublet structures are observed at ~413.5 meV in (a) and (b), corresponding to A_2^O,X and A_1^O,X respectively. To demonstrate that these are not the same transitions, a higher resolution spectrum of this region for a sample containing both the A_1 and A_2 acceptors is shown in Figure 24(b). The doublet further resolves as four lines (a,b,c,d) with the 'c' line as the strongest feature. This substructure is identical for A_2^O,X and A_1^O,X, and so we observe a superposition of the two sets of lines, displaced by 41 μeV. Using the 'c' line as

a reference, the spectral positions of the different acceptor A^O,X are 413.624±0.005 and 413.665±0.005 meV for A_1 and A_2 respectively.

Exceptional resolution is required in order to distinguish these two acceptors in the A^O,X principal transition. However, the 2S two-hole replica of the two neutral-acceptor-bound exciton (A^O,X 2h) species can be clearly separated as shown in Figure 24(a).

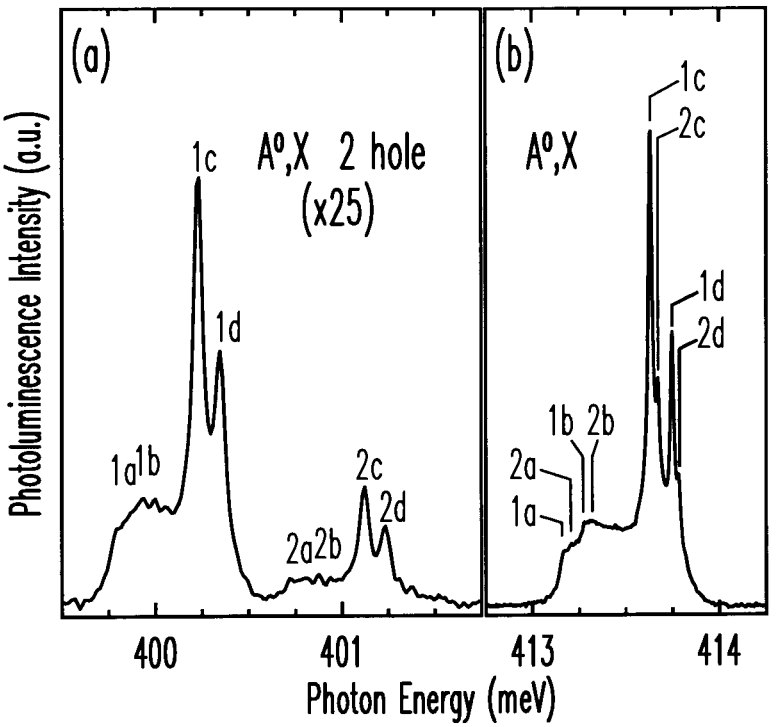

Figure 24. A higher resolution (0.02 meV) spectrum of the neutral-acceptor-bound exciton (A^O,X), showing the principal transitions (b) and the two-hole transitions (a). Four lines are seen for each acceptor in the principal transition, and are replicated in the two-hole transition. For acceptors A_1 and A_2, the lines are labelled (1a, 1b, 1c, 1d) and (2a, 2b, 2c, 2d) respectively, and Table IV contains their spectral positions. The spectrum of (a) has been expanded vertically by a factor of 25 with respect to (b).

Not only are the structures identical between the principal and the two-hole transitions, but they are also identical for the two acceptors A_1 and A_2, which shows that this structure is due entirely to a splitting of the initial state of the neutral-acceptor-bound exciton (Figure 10 on page 24). In other direct-band-gap semiconductors, this splitting is un-

derstood in terms of excited states of the hole-hole interaction, perturbed by the coexisting electron in the A^O,X complex [21]. A correspondence to that model is not possible at this point because of the strange behaviour of the two lowest energy lines. Not only are these lines broader than expected, they also disappear in the presence of magnetic field (see Figure 28). The determination of the origin of the four A^O,X lines therefore requires further analysis, beyond the scope of this thesis.

The final state of the *principal* transition (A^O,X) leaves the acceptor in its $1S_{3/2}$ ground state (Figure 7 on page 20) whereas the *two-hole* transition (A^O,X 2h) leaves it in a $2S_{3/2}$ excited state. Hence the specific acceptor $1S_{3/2}$ to $2S_{3/2}$ energy difference ΔE_{12} can be measured from the photoluminescence spectrum to high accuracy. From Figure 24 we obtain

$$\Delta E_{12}(A_1) = 13.275 \pm 0.010 \text{ meV}$$

$$\Delta E_{12}(A_2) = 12.542 \pm 0.010 \text{ meV}.$$

These values are in relatively good agreement with effective mass theory calculations [16] (summarised in Table II, page 20) which give

$$\Delta E_{12}(\text{theory}) = 11.31 \text{ meV}$$

for acceptors in InAs.

Furthermore, using the effective mass value for the $2S_{3/2}$ binding energy, 5.00 meV (ignoring any central cell effect), and the measured ΔE_{12} values, we obtain estimates for the acceptor binding energies of

$$E_{BA}(A_1)=18.28\pm0.01 \text{ meV}$$

$$E_{BA}(A_2)=17.54\pm0.01 \text{ meV}.$$

These values can be compared with the values obtained from the respective extrapolated low energy edge of the DAP (E_{DAP} for infinitely distant pairs), 396.5±0.1 meV and 397.1±0.2 meV. From equation (4.1),

$$E_{BA} = (E_{Gex} + E_{Bex}) - E_{BD} - E_{DAP}(r \to \infty) \tag{4.2}$$

where E_{Gex} is the excitonic band gap and E_{Bex} is the exciton binding energy. We substitute the measured excitonic band gap (discussed below) with the above values for the acceptor-specific quantities, and effective mass binding energies [15] E_{Bex}=1.10±0.06 meV and E_{BD}=1.53±0.08. The resulting values for the acceptor binding energies are

$$E_{BA}(A_1) = 18.72\pm0.24 \text{ meV}$$

$$E_{BA}(A_2) = 18.12\pm0.34 \text{ meV}.$$

One possible candidate for the A_1 or A_2 acceptor species is zinc. Photoluminescence measurements of GaAs grown using the same TBA source determined the presence of residual zinc acceptor impurity.

Acceptor A_3

The A_3 acceptor's donor-acceptor pair band (DA_3P) is seen each time the line labelled in Figure 22 as its neutral-acceptor-bound exciton (A_3^O,X^γ) is present. We also correlated the existence of both these features with samples that were grown following

InGaAs growths in the same reactor chamber. From the latter we postulate that A_3 is a double acceptor formed by a gallium atom on an arsenic lattice site (Ga_{As}). The A_3^O,X^γ line however, looks nothing like the corresponding A^O,X lines for acceptors A_1 and A_2. It is much broader and much deeper than the other lines (the A_1 and A_2 lines are 41 μeV apart and the A_3 line is 3.6 meV deeper). Figure 23(b) shows that its power dependence is that of a bound exciton process. We propose that this might be the signature of double-acceptor whose ground state is split, as reported in germanium for the zinc impurity [22] (there the corresponding line is labelled with the Greek letter γ). The recombination of the exciton bound to the neutral double-acceptor A_3 leaves the acceptor in the "excited" ground state, which is short-lived as it relaxes to the "true" ground state and hence the broad linewidth of the A_3^O,X^γ transition.

In this model a sharp transition to the "true" ground state should still exist, but none is observed in Figure 22(b). It is possible that this line is hidden under the A_1 acceptor line but this is unverified as we had no InAs sample containing only the A_3 acceptor. The splitting of the neutral A_3° ground state would then be ~3.6±0.5 meV. As we did for the other two acceptors, using the extrapolated low energy edge of the DA_3P band, 391.3±0.5 meV in equation (4.2), we obtain

$$E_{BA}(A_3) = 23.4\pm0.7 \text{ meV}$$

as an estimate to the A_3 acceptor binding energy.

Table III. Physical quantities obtained from the InAs spectra presented in this thesis. The unit of energy is meV

	Symbol used in document	Measured quantity
Excitonic band gap energy	E_{Gex}	415.65±0.01
Band gap energy	E_G	416.75±0.07[a]
Acceptor A_1 binding energy	E_{BA}	18.28±0.01[b]
		18.72±0.24[c]
Acceptor A_2 binding energy	E_{BA}	17.54±0.01[b]
		18.12±0.34[c]
Acceptor A_3 binding energy	E_{BA}	23.4±0.7[c]
A^O,X binding energy		2.49±0.05
D^O,X binding energy		0.42±0.02
Longitudinal optic (Γ) phonon energy		30.05±0.01[d]
Conduction band effective mass	m^*/m_0	0.026±0.002
Conduction band *g*-factor	g_c	-15.3±0.2

[a] Using an exciton binding energy of 1.10±0.06 meV [15]
[b] Using an acceptor $2S_{3/2}$ binding energy of 5.00 meV [16]
[c] From equation (4.2)
[d] From reference [1]

In summary, we have found evidence for three distinct acceptors and we estimated the acceptor binding energies using two methods: one using the two hole transitions of the A^0,X and the other using the DAP bands. The results are listed in Table III along with other physical quantities measured from the spectra of InAs detailed below. The next two sections deal with the identification of the free exciton and the donor-bound exciton features close to the excitonic band-gap region of the spectrum.

FREE EXCITON (POLARITON)

In direct band-gap semiconductors, free excitons and photons are strongly coupled where the exciton dispersion curve would have crossed the light curve in the absence of coupling. This creates both photon-like and exciton-like states collectively called

"polaritons". Because of this strong coupling, the free exciton (from now polariton) is readily measurable by reflectance (or transmittance) spectroscopy.

The excitonic energy region of InAs measured by reflectance, transmittance and photoluminescence at 1.4 K is shown in Figure 25. The now familiar structure of the neutral-acceptor-bound exciton (A^O,X) is shown in the photoluminescence curve as a point of reference only. The neutral-donor-bound exciton structure (D^O,X) will be discussed in the next section. What this figure stresses is the lack of evidence for the polariton (X) in the photoluminescence spectrum, while it is clearly observed by reflectance and transmittance (plotted as absorbance=1/transmittance). We define the minimum of the reflectance feature as the excitonic band gap E_{Gex} = 415.65±0.01 meV (For comparison, the energy at which the almost vertical portion of the curve crosses the baseline reflectance is 415.71±0.01 meV).

It seems likely that given the large radius for free excitons in InAs[†] (76 nm), together with the relatively substantial donor population even in these high-purity samples (at Nd=2.5x10^{14} cm^{-3}, the average donor separation is 170 nm), that the capture time of polaritons onto donor impurities might be much shorter than the radiative lifetime. Hence essentially no recombination from polaritons is observed in photoluminescence, at least under the 1.4 Kelvin, zero magnetic field conditions described here. It is in principle possible to use a strong enough excitation to saturate the donor sites, and thus create free

[†] The exciton radius is taken as the Bohr radius obtained from the spherical part of the exciton Hamiltonian (equation (2.9)). The reduced mass was taken from [15], using a different value for the diectric constant of 14.55±0.05 from [23].

excitons, but the linewidths at those excitation densities are apparently larger than the donor-bound-exciton binding energy, making the distinction impractical.

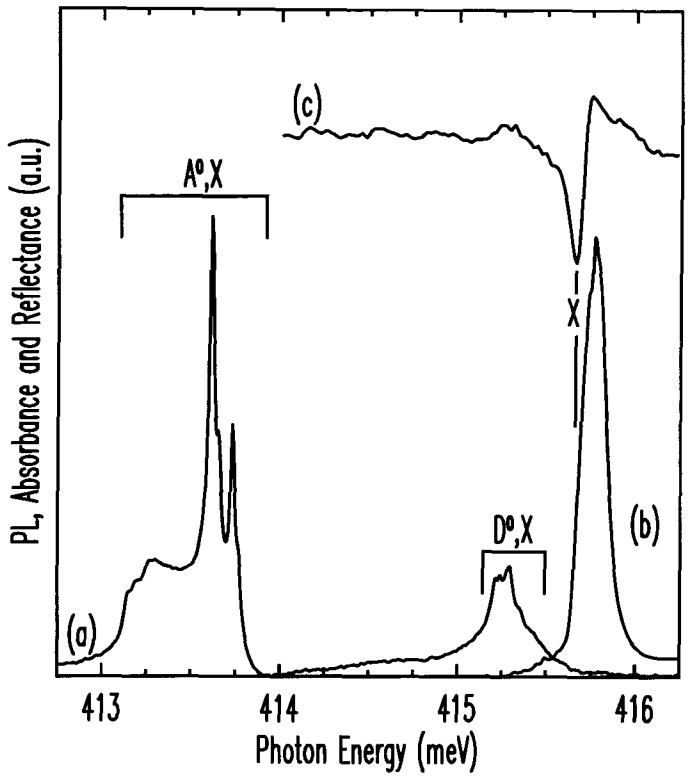

Figure 25. An expanded view of the excitonic energy region. The photoluminescence spectrum in (a) does not show the polariton (X) which clearly dominates the absorbance spectrum (b) and the reflectance spectrum (c).

As will be discussed in the next section, the donor-bound-exciton binding energy is approximately 0.42 meV. At a temperature of 4.2 Kelvin the thermal energy of the lattice (kT=0.36 meV) is enough to strongly dissociate the bound excitons so that some recombination of free excitons occurs. The photoluminescence spectrum in the excitonic energy region at the temperatures 1.4 and 4.2 Kelvin are compared in Figure 26. In this sample, the D^{O},X line is more prominent, and some evidence of the polariton is seen even at 1.4 K as a small shoulder (X) in subfigure (b). At 4.2 K, in (a), this shoulder increases substan-

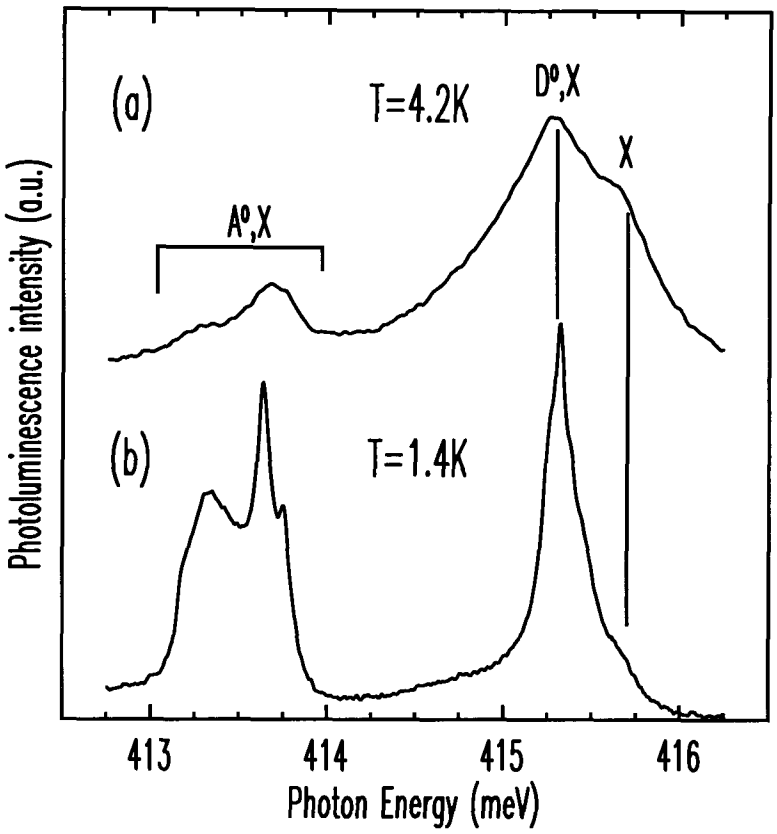

Figure 26. Excitonic photoluminescence at a) 4.2 K and b) 1.4 K showing the shift in relative intensity between X and D^0,X.

tially in intensity relative to the bound exciton features as expected from the above argument.

The drastic degradation of the photoluminescence features in going from 1.4 to 4.2 Kelvin shown in Figure 26 is likely one of the reasons why such detail in the photoluminescence of InAs was never reported before us [1].

With the help of reflectance and transmittance measurements, as well as temperature dependence photoluminescence, we have clarified that the peak above the acceptor-bound excitons in the photoluminescence spectra, is due to donor-bound excitons rather than polaritons. All the binding energies are measured relative to the band gap, which is

obtained from the polariton energy. This identification was therefore a very important one. It is further supported by magnetic field measurements discussed later in this chapter.

DONOR-BOUND EXCITONS

From the transport measurements on the samples grown simultaneously on GaAs Dr. Watkins' group obtain residual donor concentrations as low as 2.5×10^{14} cm^{-3}. This is only below the Mott transition for InAs (5×10^{14} cm^{-3} according to [4]) by a factor of two. (Above the Mott transition, the donor electron wavefunctions overlap, and the material becomes metallic). Thus the concentration of donors is still effectively quite high in these samples, and donor-bound exciton absorption is readily measurable by transmission spectroscopy. In fact all of the photoluminescence features due to donor-bound exciton recombination can be seen as absorption lines in the transmission spectrum. This was a subject of confusion in earlier interpretations[‡].

Figure 27(a) shows in detail the photoluminescence and (b) the transmittance of the neutral-donor-bound exciton feature (D^O,X). (The inverse of Figure 27(b) was plotted in Figure 25(b) as absorbance.) It is not possible to know yet if any of this structure is due to the presence of different donors, although chemical shifts (central cell effects) would be expected to be very small. Seven lines are resolved in the figure and are labelled by the letters 'a' to 'g'. The 'a' line, which is the deepest photoluminescence peak, corresponds

[‡] In ref.[1], D^O,X absorption features were erroneously attributed as due to polariton reflectance. The feature labeled as the polariton (X) in that paper was actually the D^O,X. These D^O,X absorptions were present in the reflectance spectrum because of the transparency of the substrate material (Burstein-Moss shift), and the fact that the polished back surface of those samples was reflecting the incident radiation along with the front surface reflected radiation. Hence those reflectance spectra were in fact the sum of reflectance and transmittance. The samples used later and in this study had unpolished back surfaces, and consequently the present reflectance spectra are free of these problems.

to the start of the absorption on the transmittance curve and there seem to be absorption features all the way up to a tenth of a meV from the excitonic band-gap. The 'c' line position is the most prominent in the photoluminescence and corresponds well with the peak of broader D^O,X lines from other samples which do not resolve the structure seen in Figure 27. The D^O,X binding energy, as measured from the 'a' line, is 0.42±0.05 meV. Lines corresponding to excited states of the neutral-donor-bound excitons have also been observed in other III-V semiconductors [25].

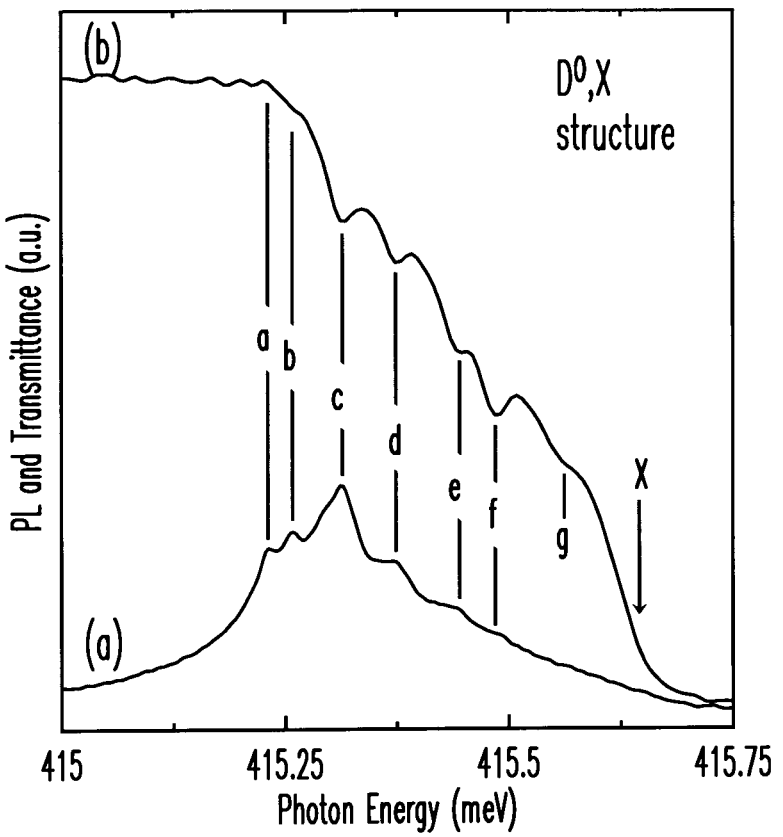

Figure 27. Substructure of the neutral-donor-bound exciton feature in the photoluminescence spectrum (a) and the transmittance spectrum (b) of the same sample. The spectral energy positions are given in Table IV. The (X) label denotes the position of the excitonic band gap.

For the purpose of reference, Table IV contains the position of most photoluminescence peaks discussed in this work and observed on InAs/InAs epitaxial layers, at 1.4

Kelvin and 0 Tesla. The table also contains the FWHM for those lines that could be resolved and a brief description of their assignment is also given.

MAGNETIC FIELD DEPENDENCE

The spectrum of InAs becomes very complicated in the presence of a magnetic field, and no thorough analysis has been undertaken at the time of this writing. The main purpose here is to support our identification of the excitonic features by showing that the polariton becomes visible in the 1.4 K InAs photoluminescence spectrum under an applied magnetic field.

We observe a linear dependence of transition energies on magnetic fields from 0.5 Tesla up to 7 Tesla. In a simple approximation, we can then describe the shift of the luminescence recombination energy by

$$\Delta E = \tfrac{1}{2}\hbar\omega_c \pm \tfrac{1}{2} g_c \mu_B B \tag{4.3}$$

where g_c is the conduction band g-factor and $\omega_c = eB/m^*$ is the cyclotron frequency. We have neglected the diamagnetic quadratic correction for simplicity and because the observed magnetic field dependence was linear to a good approximation. Using the definitions of μ_B and ω_c, one can write

$$\Delta E = \mu_B B(\frac{m_0}{m_e^*} \pm \frac{g_c}{2}). \tag{4.4}$$

Figure 28 shows part of the excitonic region under an applied magnetic field of 1 Tesla. The features labelled with an asterisk (*) correspond to spin -1/2 electron states

and those with no asterisk to spin +1/2 states. The photoluminescence (a), the transmittance (b) and the reflectance (c) are plotted on the same energy scale.

Table IV. Epitaxial InAs. Photoluminescence peak positions, assignments and references at 1.4K and 0 Tesla.

Peak position (meV)	FWHM (meV)	Symbol used in document	Assignment and comments
374	24	B_2	Deep broad band with sharp high energy edge and exponential tail. Unknown process. See Figure 30.
383.2 383.5	- -	A°,X LO (c) A°,X LO (d)	Recombination of a neutral-acceptor-bound exciton with the emission of a longitudinal optic phonon. These lines are replica of the A_1^O,X (or A_2^O,X) (c) and (d). See ref. [1]
391.3±.5 396.5±.1 397.1±.2	2.4 1.8 1.9	DA_3P DA_1P DA_2P	Donor-acceptor pair recombination with each of the three observed acceptors A_1, A_2 and A_3. Since these lines blue-shift and broaden with increased excitation, the energies given are the best estimates for infinitely distant pairs, obtained by extrapolating the low energy edges. See Figure 22 and Figure 23.
400.23 400.35 401.12 401.23	0.05 0.05 0.05 0.05	A_1°,X 2h (c) A_1°,X 2h (d) A_2°,X 2h (c) A_2°,X 2h (d)	Recombination of a neutral-acceptor-bound exciton, leaving the acceptor in a $2S_{3/2}$ excited state. The lines are replica of the A^O,X (c) and (d) lines for acceptors A_1 and A_2 and originate from the same initial state of the bound exciton. See Figure 24(a).
410.9	2.0	A_3°,X^γ	Broad, neutral-acceptor-bound exciton recombination at the A_3 acceptor impurity, possibly a double-acceptor Ga_{As}, left in the higher energy state of a split ground state. See Figure 22(b).
413.16 413.20 413.27 413.31 413.63 413.67 413.75 413.78	- - - - 0.05 0.05 0.05 0.05	A_1°,X (a) A_2°,X (a) A_1°,X (b) A_2°,X (b) A_1°,X (c) A_2°,X (c) A_1°,X (d) A_2°,X (d)	The principal transition of the neutral-acceptor-bound exciton. Four substructure lines are resolved and labelled from (a) to (d). The (c) line is the strongest feature. This substructure is identical for the A_1 and the A_2 acceptor. See Figure 24(b).
415.23 415.25 415.31 415.37 415.44 415.49 415.56	- - - - - - -	D°,X (a) D°,X (b) D°,X (c) D°,X (d) D°,X (e) D°,X (f) D°,X (g)	The principal transition of the neutral-donor-bound exciton. Seven substructure lines are resolved and labelled from (a) to (g). The (c) line is the strongest feature. See Figure 27.
415.65	-	X	The free exciton (polariton). This feature is difficult to observed in photoluminescence (see text), but can readily be seen in the reflectance spectrum. See Figure 25.

A strong polariton peak is now present in the photoluminescence spectrum and this peak lines up with the lowest of three polariton features (X_1, X_2 and X_3) observed in the reflectance and transmittance spectra (the exact nature of this polariton splitting is beyond the scope of this thesis). The large increase in free-exciton recombination under applied magnetic field is explained by the resulting compression of the free exciton and donor wavefunctions (in a classical physics analogy, the electrons are forming tighter orbits), coupled to an increase in their binding energies. This leads to a reduced capture rate by the shallow donor impurities.

It should also be mentioned that the acceptor-bound exciton 'a' and 'b' lines disappear under the application of a magnetic field so that in Figure 28(a), the A^O,X and A^O,X* structures are composed of only the 'c' and 'd' lines of acceptors A_1 and A_2. (This will require further investigation in the context of splittings of the neutral-acceptor-bound exciton complex.)

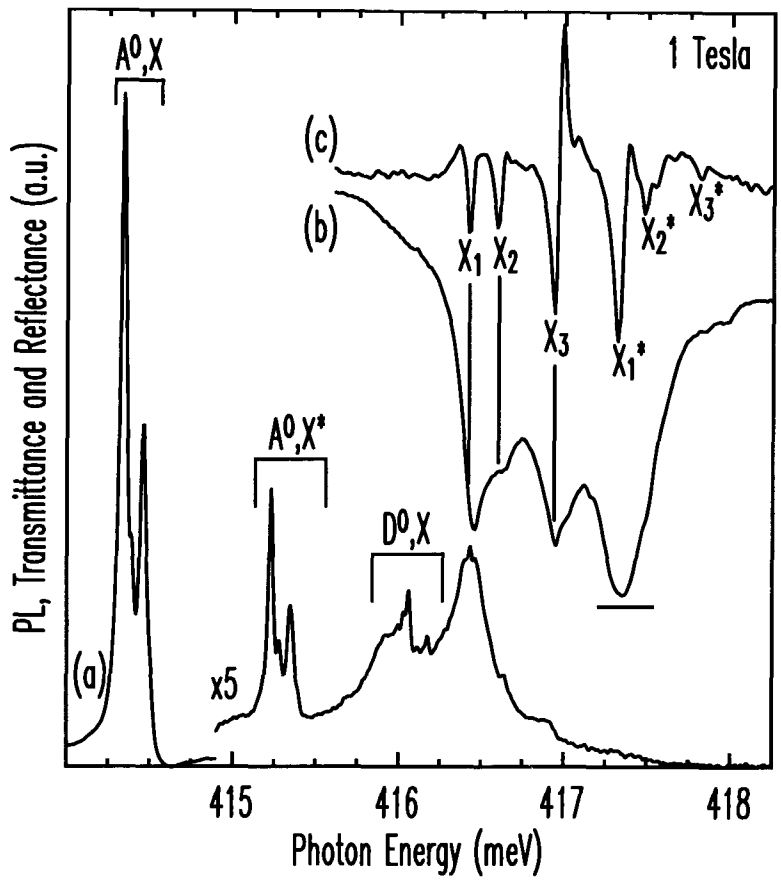

Figure 28. The excitonic region at 1.4K under a magnetic field of 1 Tesla. (a) The photoluminescence, (b) the transmittance , and (c) the reflectance. The photoluminescence shows a peak at the polariton energy, about 0.4 meV above the main D^0,X feature, which lines up with the transmittance and reflectance of the lowest lying polariton feature (X_1). The asterisk (*) labels states of opposite electron spin from those without asterisk. The zero of the transmittance spectrum has been shifted vertically for clarity, and is indicated by a horizontal line under the X_1* transition. The magnetic field splits the polariton into three main substructures (neglecting spin), which are labelled X_1, X_2 and X_3

Using equation (4.4), the spectral positions of X_1 and X_1* lines at 1 Tesla yield values of $0.03m_0$ and -15 for the electron effective mass and the *g*-factor respectively. Measurements at 7 Tesla, where our linear approximations are more valid, give $0.026\pm0.002m_0$ for the effective mass and a *g*-factor of -15.3 ± 0.2 in reasonable agreement with tabulated values [23][24] of $0.024m_0$ and -15. These agreements simply confirm the identification of the features labelled in Figure 28, which in turn support our assignments of the excitonic features at zero magnetic field.

BROAD BANDS

Broad band luminescence can arise from several mechanisms, and some processes, such as the donor-acceptor pair band, give intrinsically broad emissions, while the effect of sample inhomogeneities will broaden the entire spectrum. In most cases it is difficult to determine their precise origin, since the effects of perturbation are not easily measured on broad featureless bands.

In chapter two we assumed nearly perfect and pure crystals, hence we did not discuss any process (except for DAP) which would give intrinsically broad features. In many studied cases however, the intrinsic features discussed so far cannot be seen due to an excess of impurities or dislocations. For example in strongly n-type material, since the Fermi level has moved into the continuum of the conduction band, like a metal, the concept of quasi-hydrogenic donor levels is lost. This is the case for our substrate material.

Figure 29 shows some of the broad bands that we have observed. The B_1 band in (a) is not always present. It is seen here in an otherwise normal spectrum of a 5 μm thick epitaxial layer grown on an InAs substrate. The other spectra shown in this figure are the result of different growth processes and are not expected to resemble the kind of spectra discussed above.

The substrate photoluminescence spectrum is shown in (d) and has features labelled S_{eh} and S_{eA}. We attribute S_{eA} to free electron to acceptor recombination (e,A^0), since the substrate donor concentration is well above the Mott (metallic) limit. The low energy tail of S_{eA} is wide enough to contain all of the identified acceptor energies. The S_{eh}

line is most probably due to band-to-band recombination (e,h). B_1, in (a) does not appear to be due to substrate photoluminescence, as its energy does not correspond to any substrate feature. In samples with thin epitaxial layers, where the excitation can create electron-hole pairs in the substrate, the photoluminescence due to the substrate can dominate the spectrum as is the case in (c) for a 0.36 μm layer grown on InAs.

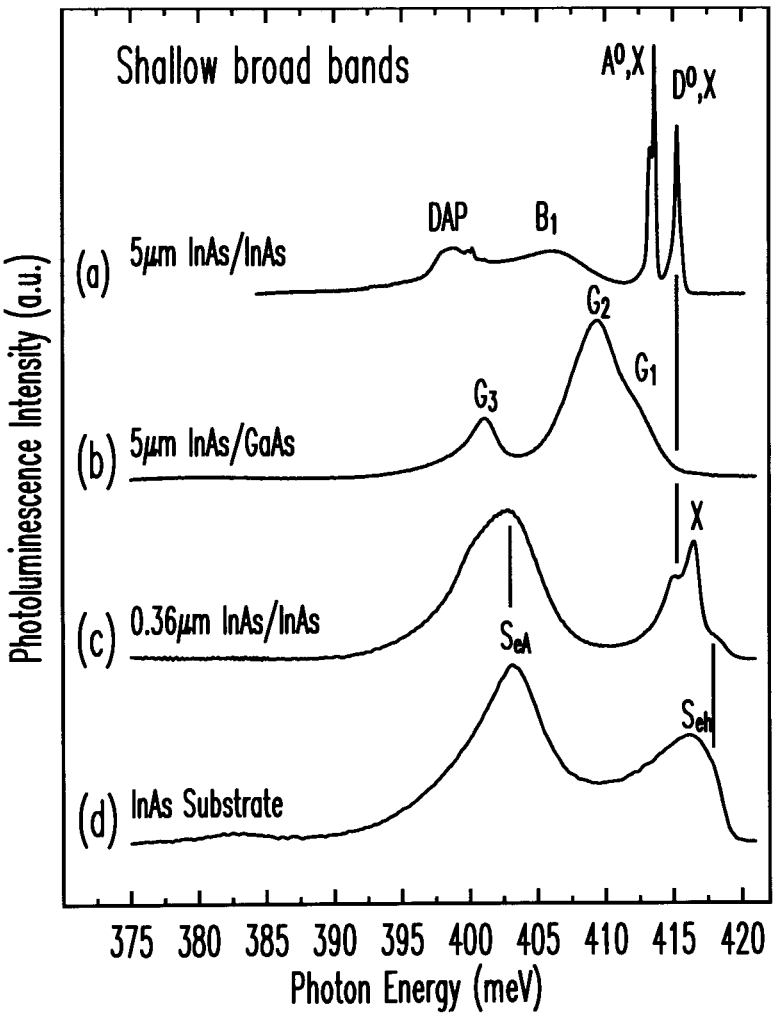

Figure 29. Photoluminescence of the various broad bands seen for different types of samples. a) An otherwise normal spectrum of InAs grown on InAs with an unidentified broad band labelled B_1 at 406 meV. b) A sample grown on GaAs showing three unidentified broad lines labelled G_1, G_2 and G_3 at spectral positions 412, 409 and 401 meV respectively. c) A thin layer of InAs grown on InAs has a spectrum dominated by substrate features. d) The spectrum of our InAs substrate material, with broad lines at 416 meV (S_{eh}) and 403 meV (S_{eA}).

An interesting observation for the 0.36 μm thick sample is that it appears to have a line at the polariton energy (X), which does not appear in thicker layers, and has a D^O,X feature but no A^O,X. This might be related to the proximity of all portions of the thin epitaxial layer to the much more heavily n-doped substrate.

Samples grown on GaAs substrates

A spectrum of one of our samples grown for transport measurements on a GaAs substrate is shown in Figure 29(b). Three broad features are visible, denoted G_1, G_2 and G_3, none of which bears any similarity to lines seen from samples grown on InAs. We have as yet no detailed explanation for the G_1, G_2 and G_3 lines. The broadeness of the lines may be due to residual strain in the relaxed layers. Other groups however, have published spectra from InAs grown on GaAs that can be reinterpreted in light of the results presented above.

The report by Tang *et al.* [7] on BME-grown InAs on GaAs substrates shows four lines which they label as 'a', 'b', 'c' and 'd'. Their 'a' line (7 meV wide, with peak at 417 meV), which they attribute to free-excitons or shallow-impurity-bound excitons resembles our substrate S_{eh} line. The position of this line, the high excitation densities used, as well as the high temperatures at which the measurements were done (11 K), leads us to suspect band-to-band recombination as a better candidate. They attribute their 403 meV 'b' line to excitonic recombination as a deep donor level. Since this line more or less corresponds to our substrate S_{eA} line, and since we saw no evidence of a process in our layers which would indicate the presence of a deep donor, we suggest that their 'b' line may be due to

free electron to neutral acceptor recombination. Their 391 meV 'c' line, which showed similar behaviour is close in energy to the donor-acceptor pair transition associated with acceptor A_3. If our postulate that this acceptor is due to a Ga_{As} impurity is correct, it is possible that a sample grown on a GaAs substrate might contain it. Finally, their 'd' line at 378 meV was attributed to a DAP transition. However we also observe a strong band at this energy, which does not exhibit DAP band behaviour.

Deep Time-Dependent Band

We have observed a deep, broad band corresponding in several aspects to the 'd' line of Tang *et al.* Figure 30 shows the power dependence of this band (B_2), in a sample for which excitonic photoluminescence intensity had significantly degraded over time. The B_2 lineshape and position are independent of excitation between 1.5 mW/cm^2 and 200 mW/cm^2, with a sharp high energy edge and a broad low energy tail. The curves for different excitations have been vertically scaled to show how the lineshape and energy position stay constant over the two decades of excitation density. We have seen no saturation of the B_2 band in this sample, however we have perhaps not followed the behaviour to as high an excitation level as did Tang *et al*, who did see a saturation of their 'd' line.

In another sample (not shown), where the B_2 band was not so prominent, we have observed a saturation, and a subsequent (not simultaneous like the case of DAP) blue-shift of this band. That sample still possessed strong excitonic photoluminescence.

In the spectra of Figure 30, the (X) denotes free-excitons created at high excitation, when the D^O,X states are saturated. The lowest excitation spectrum also resolves

D^O,X, A^O,X, and a weak DAP band. Another deep process (labelled B_3) is seen on top of the B_2 band and seems to saturate at the same rate as the bound exciton features. The integrated photoluminescence intensity dependence of the B_2 band on laser excitation density was found to be nearly linear for the range given above.

This behaviour, characterised by the band-edge luminescence losing intensity, is recoverable. Some samples were seen to have little or no band-edge luminescence one week, and then to have bright and sharp luminescence the next. When the samples show weak band-edge luminescence the B_2 band is present, while when the sample shows strong excitonic photoluminescence, in most cases B_2 is absent. What is even more surprising is that this switching in intensity between the B_2 band and the band-edge luminescence was also observed on the substrate material. This implies a fundamental, perhaps surface-related, property of InAs, which to our knowledge has not been previously reported. Theys *et al* [8] report a process of hydrogen passivation in which they see a photoluminescence line (labelled 'c' there) disappear after either deuteration, annealing, or both. This line, although different in shape, is close to the B_2 band energy.

We are unable to determine the origin and characteristics of this process as yet. Because the time scale of this behaviour is several days or more, it is not practical to keep the samples at 1.4 Kelvin. Therefore, a thermal cycling between cryogenic and room temperature is unavoidable, and may play a role in this effect.

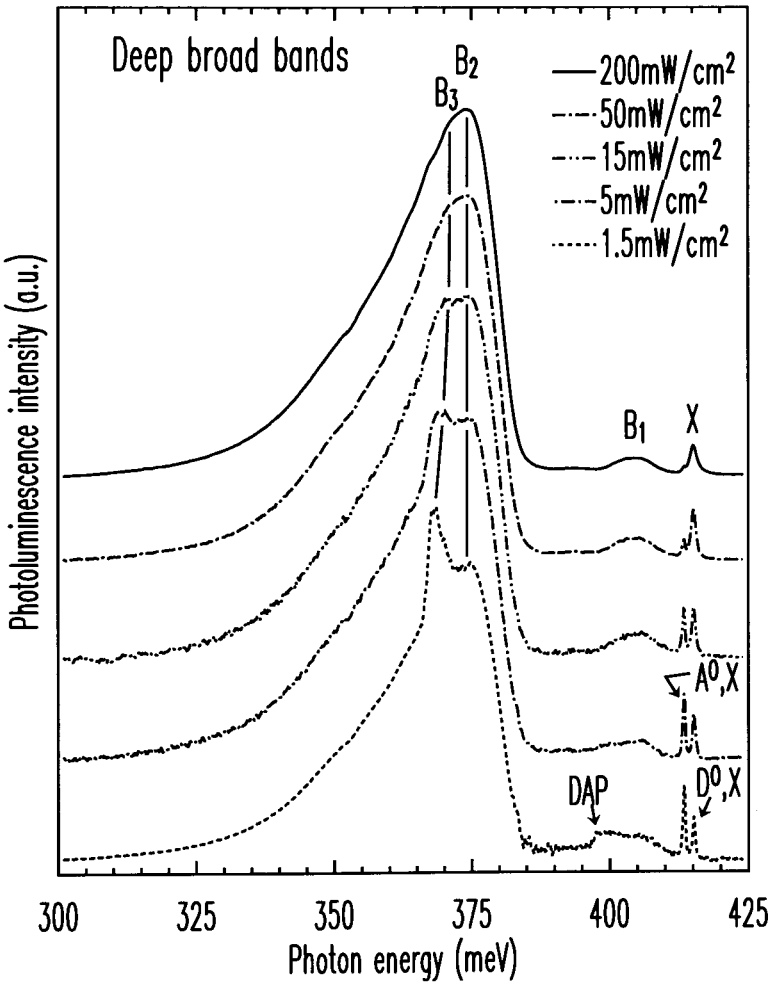

Figure 30. Excitation density dependence of the deep 374 meV band labelled B_2. The integrated photoluminescence intensity dependence from these curves is nearly linear. The B_1 band of Figure 29(a) is also seen in this spectrum, as well as a deeper transition which saturates at the rate of the bound-exciton features and is labelled B_3. The (X) labels free-excitons created at high excitation after saturation of the donor-bound-exciton states.

Out of five samples that had degraded and were left undisturbed at room temperature for several months in an inert helium atmosphere, only one still showed the B_2 band, and all of them had regenerated a strong excitonic luminescence. We also observed a full cycle of this bleaching effect for samples inside a helium filled (gas or liquid) cryostat over a few weeks, so that surface reactions with ambient gases such as oxygen or water vapour seem less likely.

Another perhaps related observation which should be mentioned, is the optical bleaching of the excitonic photoluminescence in the presence of high magnetic fields. When the samples are subject to magnetic fields above 3 Tesla, a large excitation (above 30 mW/cm^2) bleaches the excitonic photoluminescence processes. It is possible that the B_2 band described above is related in some way to this optical bleaching, but we have not investigated this possibility.

RESULTS SUMMARY

We have shown and interpreted the low temperature photoluminescence spectrum of high purity InAs grown on InAs. We have obtained, from our identifications, a number of physical quantities which had not been measured previously. Most of these quantities are listed in Table III, and a list of photoluminescence peak positions at 1.4 K and 0 Tesla is supplied in Table IV. More research will be required in order to identify the exact elemental species of acceptors A_1 and A_2, as well as to provide supporting evidence for the assignment of the acceptor A_3 to a Ga_{As} double acceptor. Using a simple treatment, we have measured the conduction band effective mass as well as the electron g-factor. More work is required in order to fully interpret our magneto-photoluminescence results measured up to 7 Tesla. The broad bands labelled B_1, B_2 and B_3 in the text still remain unexplained, and the time-dependent correlation between B_2 and the weakening of the band-edge photoluminescence should be researched further.

CHAPTER 5 - CONCLUSIONS

There are many aspects of this research that can, and must be pursued further. It is important to realise that the amount of information put forward with this thesis on the properties of InAs, has its equivalent in dozens of research papers over the span of a decade for GaAs. Hindsight has had an important role in this. It is also due in part to the better characterisation tools available today, and to having had access to both a state-of-the-art MOCVD growth facility and a world class semiconductor photoluminescence research facility. This enabled a fast response time between growth and characterisation, which is critical for the realisation of the ultra-high purity InAs layers which were essential to this study.

The experimental results themselves are summarised in the last section of chapter four. But where these results stand in the larger picture is what will be addressed here.

INAS HIGH MOBILITY APPLICATIONS

Intrinsically, InAs has high electron mobility (for comparison, the typical electron mobilities measured at room temperature for InAs, GaAs and Si are 30000, 10000 and 1500 cm^2/Vs respectively). But this does not mean that every InAs semiconductor possesses high mobility. The extrinsic scatterers such as dislocations and impurity play an important role. In order to control the inclusion of these scatterers, a study such as pre-

sented in this thesis is of high value, since it will lead to the identification of impurities which can then be traced back to the growth sources, or fabrication methods, and perhaps eliminated.

Already the high mobility quality of InAs is being put into application for Hall sensors. The sensitivity of such devices is directly related to the mobility, since they measure induced currents from weak magnetic fields.

InAs in Infrared, Opto-Electronic Applications

InAs, as a constituent of ternary and quaternary compounds is already overwhelmingly present in epitaxial opto-electronic applications. Heterojunction bipolar transistors, photoreceivers, quantum well lasers, and countless other devices make use of the InGaAs, or InGaAsP technology. There is also a recent report from Fujitsu Labs [26] of an InAs quantum-dot based optical-memory structure.

For most InGaAs structures, the role of indium is to tune the band gap of GaAs, for which the properties are well known. However, there are other alloys such as InAsSb, which are beginning to emerge in mid-infrared applications. For these, the properties of InAs are central at one extreme, and those of InSb at the other. The characterisation work which this thesis presents should be of importance to researchers presently involved in the development of these infrared devices. The knowledge of impurity contents from the understanding of the photoluminescence of InAs is an obvious tool which up to now was only available for other compounds.

WHERE TO GO FROM HERE

As mentioned in the forward to this chapter, there are countless directions in which this work can be continued, and I shall only mention a few.

Exciton Physics

There is still much information on the physical properties of InAs that can be extracted from the results of experiments performed under magnetic field. The structure of the neutral-acceptor-bound exciton, for example, is further split at high magnetic field and it should be possible to infer the mechanisms associated with the individual lines. This type of calculation has been done for other semiconductors and so the theoretical framework is already in place. The same is true for the neutral-donor-bound exciton, for which we reported several lines shown in Figure 27. The complicated structure of the polariton, shown in Figure 28, gets even more complicated at higher fields. Fits to existing models should also yield more information on the band structure.

Impurity Identification

An obvious next step in the characterisation would be to try and determine the exact species of the donor and acceptor impurities present, by intentional doping. A likely choice for one of the acceptor impurities A_1 or A_2, as mentioned before, is zinc since GaAs grown using the same As source showed weak photoluminescence emission due to residual zinc. It should also be straight forward to verify the postulate of a Ga_{As} double acceptor impurity for A_3, since Ga sources are readily available and could be used to contaminate an InAs growth.

Ion implantation doping of several species has been attempted, but the effect of annealing the InAs (to recover from the damage) seemed to be larger than the effect of the different doping species. Perhaps a larger bombardment flux may be required.

InGaAsSb and Related Compounds

Some debate remains regarding an *anomalous band gap* in As-rich InAsSb, as well as the band alignments in InAsSb/InGaAs and other related heterostructures [27]. The photoluminescence study of carefully designed quantum well structures can perhaps elucidate some of the questions. The availability of the cryogenic interferometer presented in this work, which has been developed for such a purpose, should yield some useful information on these heterostructures.

But material purity remains a problem to date. As explained in chapter four, the donor concentration metal-insulator transition is directly dependent on the carrier effective radius. Like InAs, InSb has a small conduction band effective mass and therefore the effective radius is very large, requiring very high purity in order to keep the Fermi level in the band gap. The work reported here is the first observation of this level of purity in InAs. No such observation has been made in InSb so far, implying that the impurity levels may still be too high.

... So there I was. I couldn't remember much. I could feel it had been rough. And I knew that somehow I had spilled my guts to them. There was nothing they didn't know. I had to leave the city. I had to leave soon...

APPENDIX A

The InAs samples were grown using the method described in chapter three. Layer thicknesses of 5μm, a growth temperature of 540°C, a TBA growth limiting partial pressure of 0.12 Torr with a TMI flow of ~100 sccm were used, unless otherwise specified. Table V lists the samples that were used in the figures of this thesis. For more information on the growth conditions, see reference [20].

Table V. List of samples used for the thesis figures.

Sample #	Distinction	Spectrum used in...
269	grown on GaAs	Figure 28(b)
393	0.36μm layer	Figure 28(c)
408	grown at 500°C	Figure 21(b), Figure 22
425	no prelayer	Figure 25
427		Figure 29
428		Figure 23, Figure 24, Figure 26, Figure 27.
305	Carbon implant, annealed	Figure 21(a)
InAs Substrate	no epitaxy	Figure 28(d)

APPENDIX B

A spectral resolution and sensitivity test was performed on the cryogenic interferometer described in chapter three. A small vacuum cell, in which water vapour was trapped at a reduced pressure, was place at the input port of the interferometer. The other side of the cell (about 15cm away and facing the spectrometer input) was covered with a low emissivity gold-plated mirror to minimise the background black body radiation. The infrared emission from the water molecules at room temperature was easily measured by the 100K background interferometer.

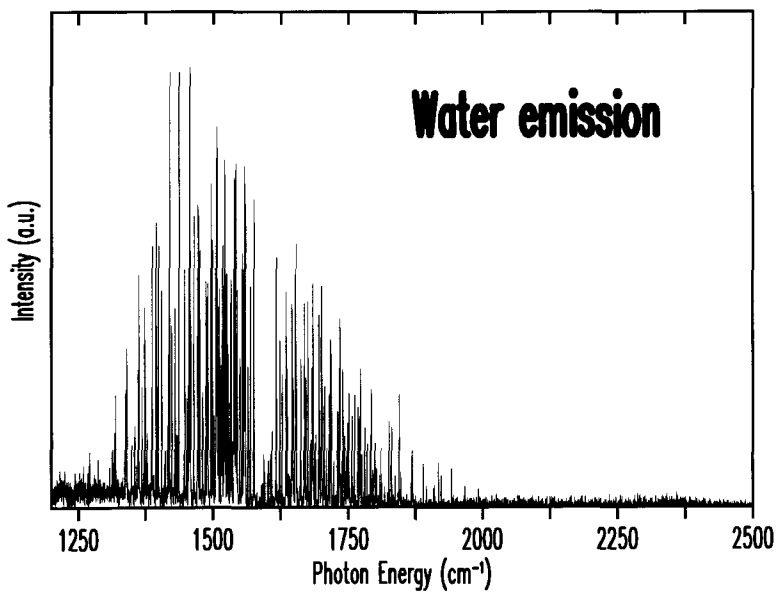

Figure 31. The mid-infrared spectrum of water, measured with the cryogenic Fourier transform interferometer, using a HgCdTe detector.

Figure 31 shows the whole spectrum, measured with a HgCdTe photodetector, and a blow-up of the same spectrum is given in Figure 32. The instrumental resolution used was nominally 0.02 cm^{-1}, and linewidths as narrow as 0.03 cm^{-1} were measured, confirming the instrumental resolution limit of the original machine, at room temperature.

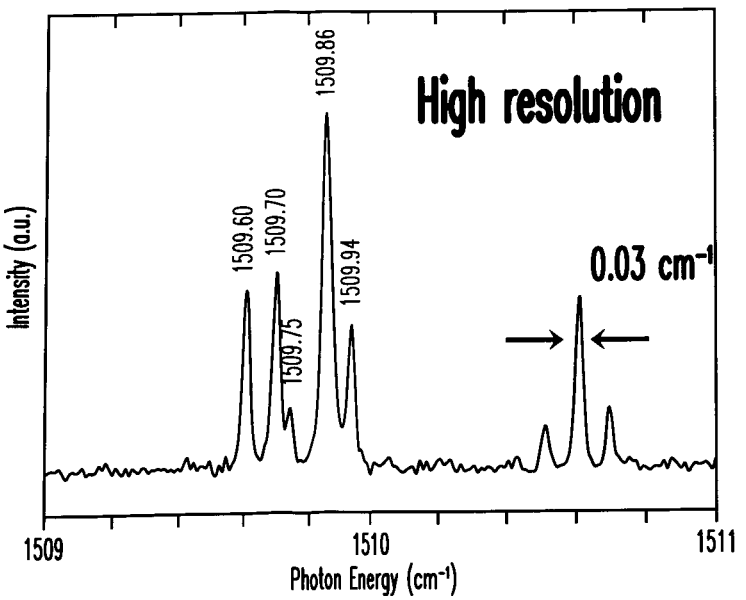

Figure 32. Blow-up of Figure 31 on a few lines to demonstrate the instrumental resolution.

REFERENCES

[1] Y. Lacroix, S.P. Watkins, C.A. Tran and M.L.W. Thewalt, Appl Phys. Lett. **66,** 1101 (1995).

[2] Y. Lacroix, S.P. Watkins, C.A. Tran and M.L.W. Thewalt, *Narrow Gap Semiconductors 1995,* Conference Series #144, Institute of Physics, Bristol, 297 (1995).

[3] Y. Lacroix, C.A. Tran, S.P. Watkins and M.L.W. Thewalt, *Proceedings to the 7th Canadian Semiconductor Technology Conference (August 14-18 1995),* accepted for publication in the Canadian Journal of Physics.

[4] R.D. Grober and H.D. Drew, J. Appl. Phys. **65,** 4079 (1989).

[5] Z.M. Fang, K.Y. Ma, D.H. Jaw, R.M. Cohen and G.B. Stringfellow, J. Appl. Phys. **67**, 7034 (1990).

[6] Z.M. Fang, K.Y. Ma, R.M. Cohen, and G.B. Stringfellow, Appl. Phys. Lett. **59,** 1446 (1991).

[7] P.J.P. Tang, C.C. Phillips and R.A. Stradling, Semicond. Sci. Technol. **8,** 2135 (1993).

[8] B. Theys, A. Lusson, J. Chevalier, and C. Grattepain, S. Kalem and M. Stutzmann, J. Appl. Phys. **70,** 1461 (1991).

[9] Y. Lacroix, C.A. Tran, S.P. Watkins and M.L.W. Thewalt, submitted to J. Appl. Phys., (1996).

[10] C. Kittel, *Introduction to Solid State Physics*, John Wiley & Sons, New York (1986).

[11] N.W. Ashcroft, N.D. Mermin, *Solid State Physics,* Holt Reinhart and Winston, New York (1976).

[12] W.A. Harrison, *Electronic Structure and the Properties of Solids*, Dover, New York (1989).

[13] J.R. Chelikowsky, M.L. Cohen, Phys. Rev. B **14**, 556 (1976).

[14] J.M. Luttinger and W. Kohn, Phys. Rev. **97**, 869 (1955).

[15] A. Baldereschi and N.C. Lipari, Phys. Rev. B **3,** 439 (1971).

[16] A. Baldereschi, Phys. Rev. B **9,** 1525 (1974).

[17] K.W. Böer, *Survey of Semiconductor Physics*, Van Nostrand Reinhold, New York, (1990), and the many references therein.